small structures
www.small-structures.com

Defect Engineering on CeO_2-Based Catalysts for Heterogeneous Catalytic Applications

Chunming Yang, Yuxuan Lu, Le Zhang, Zhijie Kong, Tianyi Yang, Li Tao, Yuqin Zou,* and Shuangyin Wang**

With abundant crystal defects, cerium oxide (CeO_2), widely used in heterogeneous catalysis, has attracted extensive attention. In recent years, researchers have investigated that the defect chemistry of CeO_2 plays a vital role in its catalytic activity and have developed various defect introduction methods to synthesize stable and efficient defective CeO_2-based catalysts. Herein, the understanding, introduction, and applications of defect chemistry in CeO_2-based heterogeneous catalysis are reviewed, and the structure–activity relationship between defect engineering and catalytic performance is recommended with great emphasis. Interests are put into the investigation of how defects influence the activity and stability of defective CeO_2 catalysts and effective strategies for fabricating efficient, stable, and defective CeO_2 catalysts. Finally, the existing problems and perspectives of CeO_2 defect chemistry for heterogeneous catalysis are displayed. This review provides a reference for in-depth understanding and the design of more efficient CeO_2-based catalysts for heterogeneous catalysis.

1. Introduction

In the past few decades, tremendous attention have been paid to heterogeneous catalysis, which plays a key role in solving environment and energy problems.[1] In heterogeneous catalysis, chemical reaction occurs at the multiphase interface between catalysts and reactants, and the kinetic processes such as adsorption, reaction, and desorption of reactants into products are the key steps that affect heterogeneous catalytic reactivity.[2] Moreover, it is worth noting that these processes are often directly related to the structural properties of catalysts.

The defect structure universally existing in solids has a great impact on the reactivity of solid materials.[3] For a material, defects can be divided into two types according to their origin: intrinsic defects and doped defects. Motti et al. clarified the intrinsic defects and their photochemistry in lead halide perovskite, and described the correlation between defects and the macroscopic properties of the material.[4] For doped defects, defect engineering, including doping, chemical reduction, high annealing, ion irradiation, and surface etching as an effective method to adjust the electronic and geometric structure of catalysts, has been widely applied in heterogeneous catalysis. Our groups have summarized the application of defective materials modified by defect engineering in electrocatalysts, rechargeable batteries, and fuel cells.[5] This is an important prerequisite for our comprehensive and in-depth study of defect chemistry.

Among defective catalysts, CeO_2, as one of the most popular rare-earth oxides, has attracted considerable attention in academia and industry on account of its abundant crystal defects and high oxygen storage capacity.[6] Recently, defective CeO_2 has been extensively applied in catalysis, especially in heterogeneous catalysis, as shown in **Figure 1**. Small-molecule oxidation reaction such as CO and methanol oxidation[7] small-molecule reduction reaction, including CO_2 and N_2 reduction[8] water splitting[9] solid oxide fuel cells[5a] photocatalysis[10] biochemical[11] organic transformation[12] and are as described as follows.

Currently, a vast number of studies have been devoted to fabricating CeO_2 and CeO_2-based catalysts. Yang et al. published an overview of recent research progress on synthesis of CeO_2-based mixed-oxide catalysts and typical applications.[6] Ma et al. reported a critical review on visible-light-response CeO_2-based photocatalysts with enhanced photodegradation of pollutants.[10a] However, a series of researches have mostly focused on the controlled synthesis of CeO_2-based nanomaterials and the possibility of different catalytic reactions, and rarely have involved the systematic study of defect chemistry on CeO_2-based nanomaterials. Thus, in this article, the understanding, introduction, and applications of defect chemistry in CeO_2-based heterogeneous catalysis are reviewed, and the structure–activity relationship between defect engineering and catalytic performance is recommended

C. Yang, Y. Lu, Z. Kong, T. Yang, L. Tao, Y. Zou, S. Wang
State Key Laboratory of Chem/Bio-Sensing and Chemometrics
Provincial Hunan Key Laboratory for Graphene Materials and Devices
College of Chemistry and Chemical Engineering
The National Supercomputer Centers in Changsha
Hunan University
Changsha 410082, P. R. China
E-mail: taoli@hnu.edu.cn; yuqin_zou@hnu.edu.cn;
Shuangyinwang@hnu.edu.cn

C. Yang, L. Zhang
College of Chemistry and Chemical Engineering
Shaanxi Collaborative Innovation Center of Clean Utilization of Low Rank Coal
Yan'an University
Yan'an, Shaanxi 716000, P. R. China

The ORCID identification number(s) for the author(s) of this article can be found under https://doi.org/10.1002/sstr.202100058.

DOI: 10.1002/sstr.202100058

 © 2021 Wiley-VCH GmbH

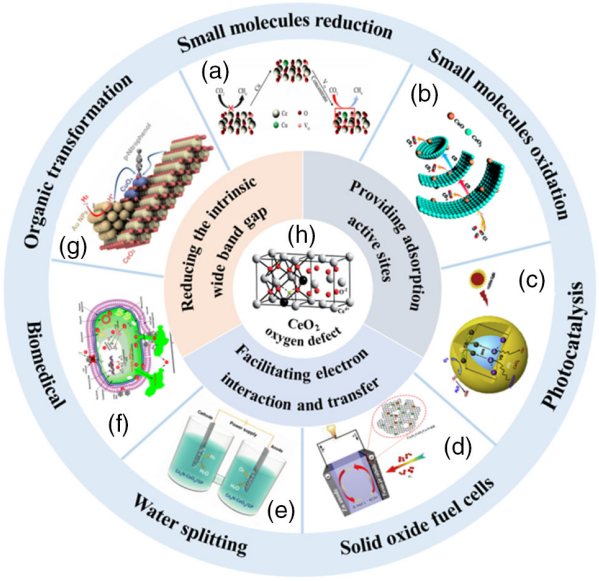


Figure 1. The basic function of defective CeO_2 catalysts and typical applications for small-molecule oxidation/reduction reaction, photocatalysis, solid oxide fuel cells, water splitting, organic transformation, and biochemicals. a) Reproduced with permission.[131a] Copyright 2021, Springer Nature. b) Reproduced with permission.[131b] Copyright 2020, Wiley-VCH. c) Reproduced with permission.[131c] Copyright 2018, American Chemical Society. d) Reproduced with permission.[131d] Copyright 2015, Elsevier. e) Reproduced with permission.[131e] Copyright 2019, Royal Society of Chemistry. f) Reproduced with permission.[127] Copyright 2018, Elsevier. g) Reproduced with permission.[124c] Copyright 2020, Springer Nature. h) Reproduced with permission.[131f] Copyright 2006, National Academy of Sciences, USA.

with great emphasis. We are committed to discussing how defects affect the activity and stability of defective CeO_2-based catalysts and effective strategies for fabricating efficient, stable, and defective CeO_2-based catalysts. Finally, the existing problems and perspectives of CeO_2-based catalysts' defect chemistry in heterogeneous catalysis provide references for the design of more efficient catalysts.

2. Structure and Defect Chemistry of CeO_2

2.1. Structure of CeO_2

The cubic fluorite-structured CeO_2 with space group Fm3m (**Figure 2**a)[13] is geared to face-centered cubic (FCC), which can maintain a similar crystal structure over the temperature range from the melting point.[14] Compared to other lanthanide oxides, such as ZrO_2, La_2O_3, Gd_2O_3, and Y_2O_3, CeO_2, with its low price, is abundant in the Earth's crust and possesses unique electronic configurations of [Xe] $4f^1$ $5d^1$ $6s^2$ resulting in excellent physical and chemical properties. Each Ce^{4+} is coordinated with eight oxygen ions nearby, and each O^{2-} in the tetrahedral space coordinates with four nearest Ce^{4+}.[15] At room temperature, pure stoichiometric CeO_2 appears pale yellow due to Ce^{4+}–O^{2-} charge transfer, instead of nonstoichiometric CeO_{2-x}, the color of CeO_{2-x} ($0 < x < 0.5$) turns blue or even black.[16] For nonstoichiometric CeO_{2-x}, each cerium atom can furnish four electrons to fill the *p* orbital of an oxygen atom, and electrons from the oxygen atom are transferred to two adjacent cerium atoms, which are reduced from Ce^{4+} to Ce^{3+}. The cerium ion in CeO_2 can realize the formation or elimination of oxygen vacancies by the reversible conversion between Ce^{4+} and Ce^{3+}.[17] The corresponding formation process of oxygen vacancies is listed as follows.

$$O^{2-} \leftrightarrow O_{\ddot{o}} + 2e^- + 1/2O_2(g) \quad (1)$$

where O^{2-}, $O_{\ddot{o}}$, and e^- are an oxygen ion on the lattice site, doubly charged oxygen vacancies, and electrons in the conduction band are composed of Ce 4*f* energy states.[18] As centers of oxygen activation, oxygen vacancies are reactive sites and the key components of oxygen storage in oxidation reaction.

2.2. Defect Chemistry of CeO_2

For the past few years, defective oxides such as CeO_2, ZnO, TiO_2, and WO_3 with excellent physical and chemical properties have gradually entered the view of researchers as described in **Table 1**. By comparison, defective CeO_2 with large potential is especially prominent. Defects in the crystal structure are caused by the displacement of atoms from lattice positions, which results in the destruction of the symmetry in the perfectly periodic lattice. As described in Figure 2b, the defect chemistry of CeO_2 has been categorized according to the dimensionality of the defects into line defects, including dislocation defects,[19] plane defects containing grain boundary defects,[20] and point defects, such as oxygen defects and cerium defects.[21]

Line defect refers to a defect in which the crystal is periodically destroyed in a line area (Figure 2c), mainly due to dislocations, which can be classified as "edge dislocation" and "spiral dislocation."[19a] Yasunaga et al. investigated the nucleation and growth process of faulted-interstitial-type dislocation loops in CeO_2 and concluded that a growth of the oxygen vacancy mobility and dislocation loops took place with descending incident electron energy.[19b,19c]

The plane defect is a plane formed in a crystal by a region deviating from periodicity, such as faulting and grain boundary, of which the grain boundary is the most widespread. Because the grains on both sides of the CeO_2 grain boundary are arranged in different directions, it possibly becomes a transition region, resulting in specific grain boundary structures and nonstoichiometry.[20b] Atoms at the grain boundary are generally higher in energy than those within the grain, and there may be vacancies, dislocations, and other defects, which often have a strongly impact on the macroscopic electrical and chemical properties of a material. Therefore, the concentration of oxygen vacancies in CeO_2 is highly correlated to the atomic structure at the grain boundary.

Among the point defects, oxygen defects with a simple structure and extensive applications in heterogeneous catalysis have been diffusely studied as opposed to the two aforementioned defects. According to their origin, the oxygen defects of CeO_2 can be systematized as intrinsic defects and doped defects. Intrinsic defects generally occur with thermal disorderness in a crystal, which can be formed by the reductive conversion of

© 2021 Wiley-VCH GmbH

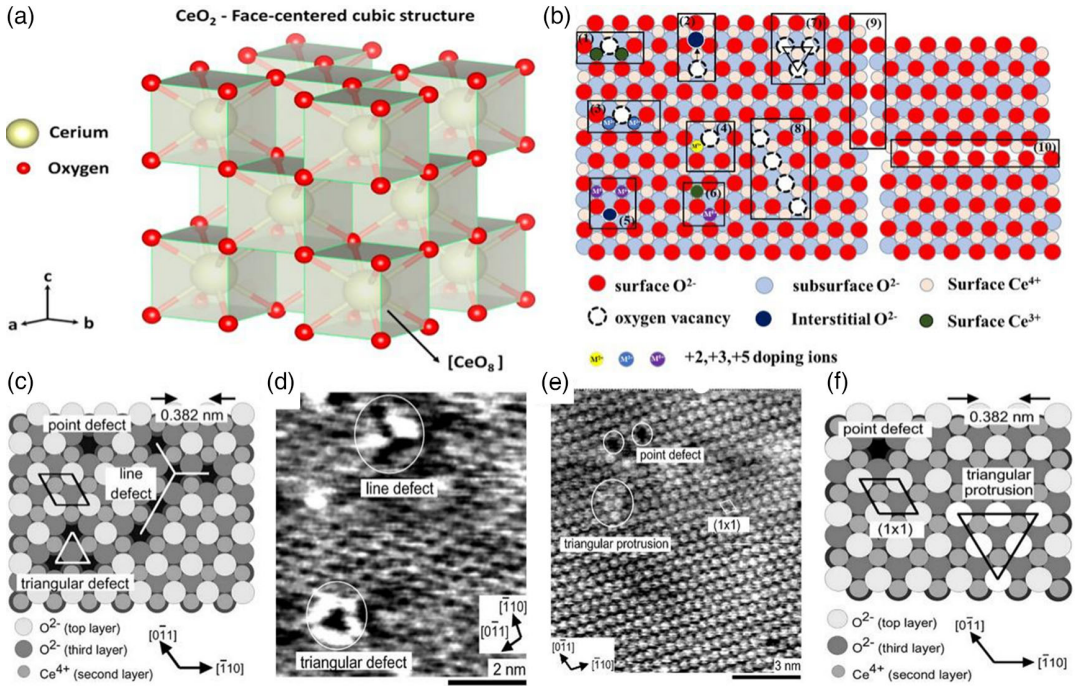


Figure 2. a) Chemical structure of the unit cell of CeO_2. Reproduced with permission.[13] Copyright 2019, American Chemical Society. b) Schematic picture of CeO_2 crystal defects. (1) Oxygen vacancy; (2) interstitial oxygen defect; (3) oxygen vacancy derived from doping of trivalent ion; (4) oxygen vacancy derived from doping of bivalent ion; (5) interstitial oxygen defect derived from doping of pentavalent ion; (6) cerium defect derived from doping of pentavalent ion; (7) triangular defect cluster; (8) linear defect cluster; (9) dislocation; (10) grain boundary. Data from ref. [19d]. c) Model of bulk-terminated structure of CeO_2 (111) with oxygen layer termination. d) Atom-resolved noncontact atomic force microscopy (NC-AFM) image of nearly stoichiometric CeO_2 (111) surface, $\Delta f \approx 149$ Hz. e) After annealing for 240 s, $\Delta f \approx 258$ Hz. f) Model of multiple defects of line defects and triangular defects observed in (e). b–f) Reproduced with permission.[24] Copyright 2002, Elsevier.

Table 1. Comparison of defective oxide catalysts in heterogeneous catalysis.

Catalysts	Advantages	Disadvantages	Refs.
CeO_2	1. High oxygen storage and release capacity 2. Excellent redox cyclicity 3. Unique electronic configurations 4. Chemical and thermal stability 5. Abundant reserves and low price	Low electrical conductivity	[6,10a]
ZnO	1. Unique electrical configurations 2. Piezoelectric 3. Ease of synthesis 4. Nontoxicity 5. Low cost		[128]
TiO_2	1. Inexpensiveness 2. Chemical and thermal stability 3. Low toxicity and desired conduction		[129]
WO_3	1. Various stable crystal structures 2. Various oxygen-deficient structures 3. Low cost, high stability, and acid corrosion resistance 4. High concentration of active sites and oxygen defects		[130]

Ce^{4+} to Ce^{3+} or the migration of lattice oxygen.[22] By contrast, doped defects derive from heteroatoms/particles replacing normal atoms/particles or occupying gap positions in normal nodes. Different oxygen defects or cerium defects are produced depending on different valence states of doped ions.[23] In nanocrystalline CeO_2, when the state of cerium in CeO_2 changes, a variety of defects can be formed on its surface, including point defects and line-type (Figure 2c,d) and triangular-type defect clusters, as shown in Figure 2e,f, resulting from multiple point defects.[24] However, there are few researches on the practical application of defect clusters in catalytic reactions, with the focusing being more on their structural characterization. Therefore, controlling the defect density of CeO_2 by a wide range of reasonable means is of great significance to the improvement of heterogeneous catalysis. Emphasis is mostly put on the introduction, characterization, and application of point defects, whereas line defects and plane defects are still rare.

3. Characterization of Defects

It is well known that the defects of nanosized CeO_2 have a great influence on heterogeneous catalysis, but the mechanism between the defect structure and catalytic activity is still unclear. Therefore, it is essential to get accurate characterization of the defect structure, in terms of clearly studying the effect of defects

© 2021 Wiley-VCH GmbH

on the catalytic activity of CeO_2. So far, the characterization methods of defective CeO_2 are mainly separated into spectroscopy characterization methods and microscopic imaging technology.

3.1. Spectroscopy Characterization Methods

Spectroscopy characterization, including X-ray photoelectron spectroscopy (XPS), electron paramagnetic resonance spectroscopy (EPR), Raman spectra, and X-ray absorption spectroscopy (XAS), allow materials to be identified and their structures determined from the spectral signals, as each structure has its own characteristic line.

XPS is a technology based on the principle of using X-ray to excite the valence electrons or inner electrons of the sample atom, and detecting the energy of the excited photoelectron to study the composition and valence state of the sample surface. The conversion of Ce^{4+} to Ce^{3+} is accompanied by the formation of oxygen vacancies. Jiang's group characterized the concentration of oxygen defects by detecting the peak area of Ce^{3+}, as shown in **Figure 3**a, and calculated the ratios of Ce^{3+} to total Ce (Ce_{total}). The CeO_2 nanorod (CeO_2 NR) with 15% Fe^{3+} iron doping is the highest.[25] This method has received increasing attention for characterizing defects in CeO_2.[26] Prior to this, there were also researchers who divided the peak of O 1*s*, determining the species of oxygen by the band energy at a particular location.[27] However, this method has some limitations due to the low reliability of semiquantitative XPS analysis and the complexity and diversity of oxygen species. Therefore, most of the current studies combine the aforementioned two to comprehensively characterize oxygen defects.

EPR, also known as electron spin resonance (ESR), is a technique to study the structure of a sample through the interaction of the electron spin magnetic moment with other parts of the sample using the electron spin magnetic moment as a probe. It is well accepted that the effect of defects on the electronic structure cannot be ignored, so it can be used to characterize the oxygen defects of nanostructured CeO_2. The EPR test in Figure 3b shows the resonance response signal of unpaired electrons in an

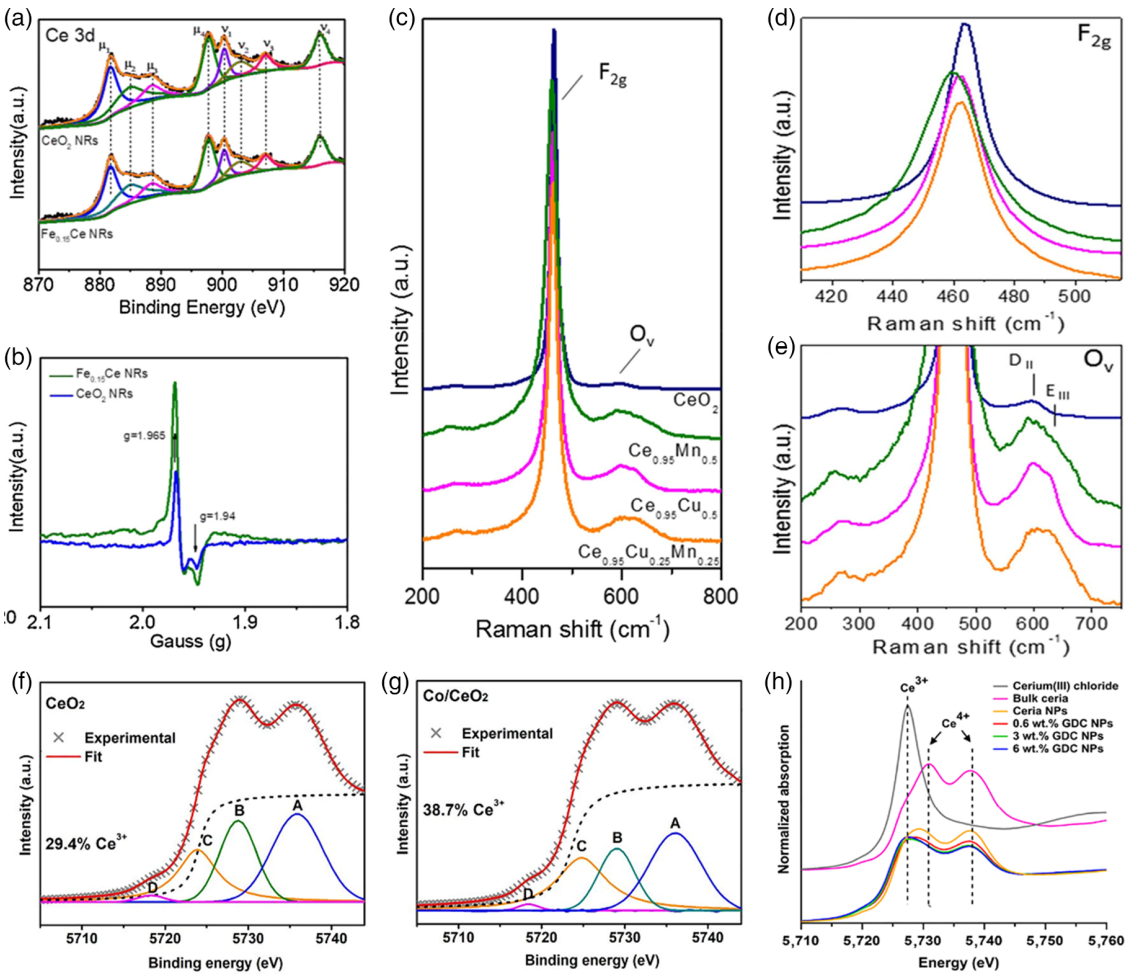


Figure 3. a) Ce 3*d* XPS spectra of CeO_2 and $Fe_{0.15}Ce$ NRs. Reproduced with permission.[25] Copyright 2020, Elsevier. b) EPR spectra at room temperature. Reproduced with permission.[24] Copyright 2002, Elsevier. c) Raman spectra of the prepared catalysts. d) Enlarged view of the F_{2g} peak. e) Enlarged view of the defect band region. c,d) Reproduced with permission.[26b] Copyright 2018, Springer Nature. f) XANES spectra fitting of the CeO_2 and g) Co/CeO_2. Reproduced with permission.[32] Copyright 2020, American Chemical Society. h) Ce L_3-edge XANES spectra of cerium (III) chloride, commercial bulk ceria, ceria NPs, and gadolinium-doped ceria nanoparticles (GDC NPs). Reproduced with permission.[33] Copyright 2020, Springer Nature.

© 2021 Wiley-VCH GmbH

applied magnetic field. It was verified by Jiang and his team that the symmetrical signals $Fe_{0.15}Ce$ NRs (1.965) present more strongly than CeO_2 (1.94),[25] which manifests a higher unpaired electron capture capability at oxygen defects in different positions.[28]

Raman spectroscopy utilizes the information of molecular vibration and rotation to detect the relative defect by analyzing different scattering spectra. The peak at 466 cm^{-1} in the Raman spectrum of pure stoichiometric CeO_2 corresponds to the symmetric contraction vibration of Ce—8O in the CeO_2 lattice in the F_{2g} mode,[29] which is sensitive to any disorder, doping, or particle-size-induced effects in the lattice caused by heating. When a large amount of oxygen vacancies is generated in the reduction of CeO_2, the F_{2g} vibration peak will shift. By analyzing the Raman shift of the spectrum, the oxygen vacancy, nonstoichiometric number, and other information of CeO_2 can be obtained.[30] Dosa et al. demonstrated the existence of oxygen vacancy by Raman spectroscopy and quantitatively measured the content, as shown in Figure 3c–e. They found that the introduction of dopants can further promote the formation of inherent defects in CeO_2.[26b]

In addition to those mentioned previously, XAS has attracted more attention in the characterization of defects in recent years.[31] As shown in the X-ray absorption near-edge structure (XANES) spectra fitting of the CeO_2 and M/CeO_2 of Figure 3f,g, Zhao et al. used XAS to analyze the species corresponding to each peak and verified the existence of oxygen vacancies in CeO_2 and transition-metal-doped CeO_2. For pure CeO_2 and Co/CeO_2 samples, the concentration of Ce^{3+} increased from 29.4% to 38.7%.[32] Moreover, soft XAS L_3-edge study clearly indicated that the changes of the dynamic valence state of Ce ions resulted from incorporation of the dopant (Figure 3h).[33]

According to the presentation of the aforementioned characterizations, it can be found that defects have a great effect on the chemical composition, electronic structure, and optical response of the material.[5a] The influence of nanosized CeO_2 defects on its catalytic activity is undoubtedly particularly great.[5d] However, the present characterization methods can only indirectly analyze the defect concentration through the signal changes of the spectral characterization results, and cannot precisely evaluate the defect concentration value. Therefore, it is of great value to find more advanced characterization means to determine the concentration, structure, and distribution of defects, which will promote the understanding of the structure–activity relationship and further improve catalytic performance.

3.2. Microscopic Imaging Technology

Other than the aforementioned spectroscopic analysis methods, the structure of defects can also be directly and clearly characterized by microscopic imaging technology. Increasing attention has been attracted by microscopic imaging technology such as scanning electron microscopy (SEM), transmission electron microscopy (TEM), atomic force microscopy (AFM), and scanning tunneling microscopy (STM). As shown in **Figure 4**a,b, based on the strength analysis of the outermost oxygen atom column in the TEM image of the (110) surface, Huang et al. found that oxygen vacancies were generated during electron beam irradiation.[34] Moreover, they characterized the microscopic distribution of defects on the surface of CeO_2 using high-resolution

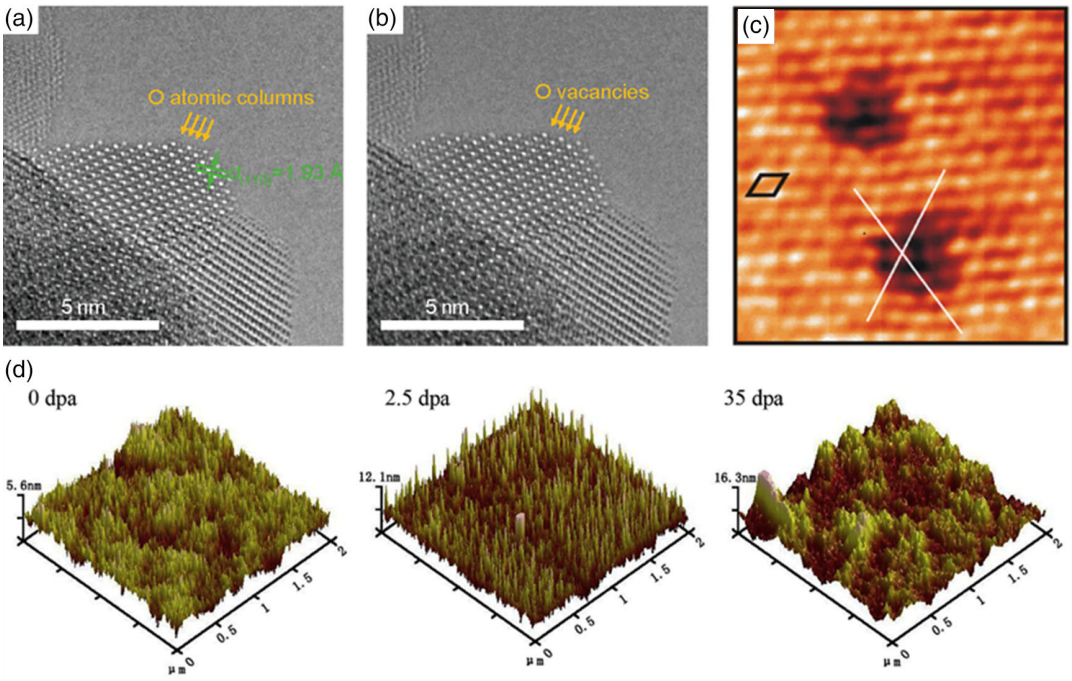


Figure 4. Aberration-corrected TEM images of the (110) surface of ceria, viewed in the (110) zone axis. a) The oxygen atomic columns at the (110) surface are labeled. b) The formation of oxygen vacancies by electron irradiation of 50 s. a,b) Reproduced with permission.[34] Copyright 2018, Springer Nature. c) STM images of oxygen vacancies of ceria films. Reproduced with permission.[35] Copyright 2006, Elsevier. d) AFM images of the as-deposited CeO_2 film, the irradiated CeO_2 films with 2.5 and 35.0 dpa. Reproduced with permission.[36] Copyright 2019, Elsevier.

© 2021 Wiley-VCH GmbH

transmission electron microscopy (HRTEM). Also, the application of STM enables oxygen vacancies to be observed directly, as shown in Figure 4c.[35] Recently, AFM has also made a big step forward in the characterization of oxygen vacancies. Chang and his team observed by in situ AFM characterization the apparent distribution of oxygen vacancies under irradiation of Au ions at different energies, as shown in Figure 4d.[36]

3.3. Dynamics Evolution of Defect Structure

In addition to the identification and characterization of defects, to further realize the rational design of atomic-level catalysts, some studies have investigated the dynamics evolution of defects in the heterogeneous catalytic process via combining the methods mentioned previously.[37] By amalgamating in situ multiwavelength Raman spectroscopy experiments with density functional theory (DFT) theoretical studies, Ziemba et al. discovered the process of oxygen disintegration and the repair of lattice vacancy in CeO_2, thus realizing an atomic-level understanding of oxygen activation on CeO_2 powder and clarifying the intimate relationship between the surface process and lattice oxygen kinetics.[37b] Schilling and co-workers also supervised real-time defect dynamics with the surface and subsurface using operando Raman/UV–vis spectroscopy. Also, they combined with the prereduction experiment under CO atmosphere, and distinctly observed the increasing defect band, gained distinct observation, which clearly demonstrates that the catalytic activity is highly dependent on the reduced state of the CeO_2 carrier.[37c] In addition, combining operando Raman and gas-phase FTIR spectroscopy, Elger and colleagues provide new insights into the mode of operation of ceria-based gas sensors during ethanol gas sensing. The spectrum of the gas-phase composition was captured using fourier transform infrared (FTIR) spectra; they directly observed changes in the oxygen vacancies in the CeO_2-based gas sensor, in combination with Raman, which could affirm the presence of oxygen vacancies.[37d] These studies demonstrate the potential of the aforementioned methods for clarifying structure–activity relationships, provide detailed views for the dynamics evolution of defect structure, and play an important role in the design of atomic-level defective CeO_2-based catalysts.

4. Strategies for Introducing Defects

In recent years, introducing surface defects depending on the second law of thermodynamics has proven to be an excellent strategy to tune the surface properties, electronic structure, and oxygen storage and release capacity, thereby improving the catalytic activity.[19b,38] Therefore, to effectively introduce oxygen defects, it is essential to understand the structure–activity relationship between defect engineering and catalytic ability as well as the internal mechanism of defect formation. Numerous methods have been explored to fabricate defective CeO_2, including doping, chemical reduction, high annealing, size and morphology control, ion irradiation, and surface etching.

4.1. Metal Doping

Doping as a common means to regulate the catalytic performance of materials has aroused great interest. The difference between the ion radius of the doped ions and the cerium will cause the lattice to expand or contract, resulting in the increase of lattice stress, and also affect the formation of defects and the migration ability of lattice oxygen. Lanthanides, transition metals, and noble metals are excellent options for doping CeO_2 to introduce oxygen defects.

Lanthanides are universally used in the doping of CeO_2 because their ionic radii are close to that of Ce. Most lanthanide metal ions are trivalent and they form nonequivalent doping with CeO_2 nanomaterials. In the CeO_2 lattice, when the trivalent lanthanide metal ions replace Ce^{4+}, an oxygen vacancy may be generated near the mixing point to balance the charge. Li et al. fabricated CeO_2-based compound oxide catalysts with M_2O_3 (M = La, Fe, and Al) and found the introduction of lanthanides indeed increases the oxygen vacancy formation capacity of CeO_2.[39] There are also some studies on gadolinium (III) (Gd^{3+}) doping of CeO_2.[33,40] It was found that the Gd^{3+} ion occupies the Ce^{4+} position of CeO_2 nanoparticles with fluorite structure. Gd^{3+}-doped CeO_2 contains a higher density of oxygen vacancy defects with the increase of Gd dopant concentrations.[33] Also, Soni et al. observed that these oxygen vacancies can generate magnetic moments on neighboring cerium ions, and the ferromagnetic coupling between the two can be explained by the F-center exchange mechanism. Once the F^+ center density reaches a critical value, the complex of Ce^{4+}–V_o–Ce^{3+} as shown in **Figure 5**a is formed. After the addition of Gd^{3+} ions (Figure 5b), the electrons captured by the oxygen vacancy occupy an orbital that overlaps with the $4f^1$ shell of the neighboring Ce^{3+} and Gd^{3+} ions, resulting in the spin polarization of Ce ions.[31] This finding provides a reference value for how to design efficient defect catalysts. Except for the effect on the magnetic moments, as for the content of Gd dopant is greater than 0.01, lattice parameters are also changed, which is attributed to the increase of the amount of both Gd^{3+} doping and oxygen vacancies.[40a] Furthermore, Sm[41] and Pr[42] with large ionic radii are also widely used in doping CeO_2 to introduce oxygen defects.

Transition metal doping, such as Fe, Co, Ni, Mn, W, and Zn, are also considered as an excellent choice to introduce oxygen defects.[25,30,32,43] Zhao and his team successfully fabricated a solid solution structure of transition metals such as Fe, Co, and Ni. By the XPS test shown in Figure 5c, the Co/CeO_2 samples showed more Ce^{3+} and oxygen vacancies than that of CeO_2 and other Co/CeO_2. These asymmetric oxygen vacancies promote the activation and dissociation of water to generate active hydroxyl groups. The detailed step-by-step hydrolysis of carbonyl sulfur is indicated by the effective action of oxygen vacancies, as shown in Figure 5d.[32] Qiu et al. constructed a system of CeO_2-induced interfacial Co^{2+} octahedral sites with rich oxygen vacancies (Figure 5e) and found that a suitable coupled p–n heterojunction interface accelerates the charge transfer between the interface of CeO_2 and Co_3O_4, which results in high oxygen vacancy concentration.[43b] The optimal Ce–Co ratio for the most excellent activity at the interface of the OER was also pointed out in accordance with Zhao's study.[32] Furthermore, Wang and Varandili's team constructed a series of CeO_{2-x} with multiple oxygen vacancies doped by single-atomic Cu.[8c,44] The experimental and theoretical results show that oxygen vacancies introduced by Cu doping have a great impact on the selectivity, activity, and Faradaic efficiency of CO_2 reduction to methane.

© 2021 Wiley-VCH GmbH

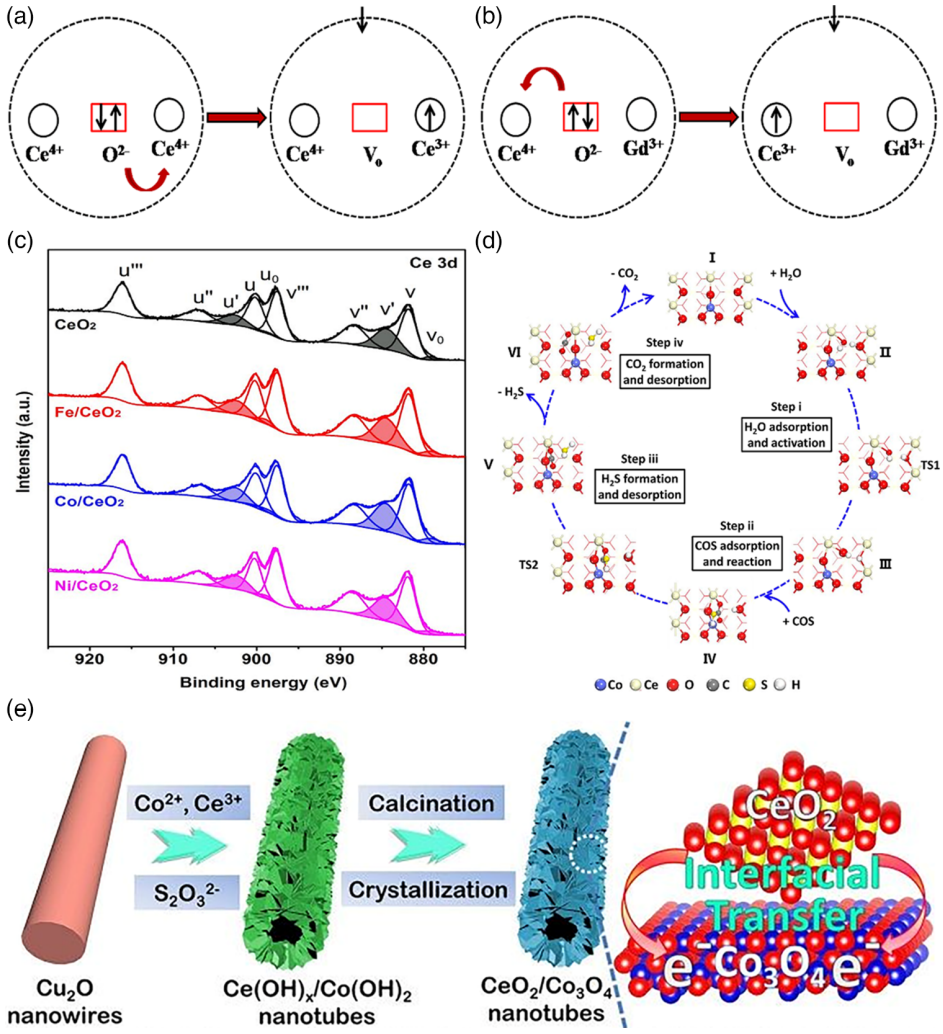


Figure 5. a,b) The complexes and mediated ferromagnetic ordering through the F^{+} center for pure CeO_2 and $Ce_{1-x}Gd_xO_2$ ($x = 0.02$, 0.04, 0.06, 0.08, and 0.10) nanomaterials. The bold inverted arrow over the circle indicates the electron left after oxygen vacancy (V_o) formation. a,b) Reproduced with permission.[31] Copyright 2015, Springer Nature. c) XPS spectra of the CeO_2 and M/CeO_2 in the region of Ce 3*d*. d) Reaction pathways for the COS catalytic hydrolysis on the surface of Co/CeO_2 and with one oxygen vacancy (Co/CeO_2–$1V_o$). c,d) Reproduced with permission.[32] Copyright 2020, American Chemical Society. e) The strong interaction between the doped metals and CeO_2 promotes the spontaneous formation of asymmetric oxygen vacancies in M/CeO_2. Reproduced with permission.[43b] Copyright 2019, American Chemical Society.

In addition to doped transition metals, noble metal doping could introduce oxygen defects to CeO_2 and improve the catalytic activity of CeO_2.[12b] Dong et al. loaded 8.7 wt% gold nanoparticles onto CeO_2 nanosheets and found that the concentration of Ce^{3+} was increased, which promoted the adsorption and activation of CO_2 and the generation of intermediates *COOH.[45] Zeng and his team synthesized a Ag-loaded CeO_2 catalyst and investigated the activity for soot oxidation. Experimental analysis indicated that a large amount of oxygen vacancies were induced by Ag nanoparticles at the CeO_2 lattice via electronic transfer. In addition, they discovered that oxygen vacancies promote to capture more oxygen species and generate the O_x species, which are vital factors to increase the activity of the Ag–CeO_2 catalyst.[46] The advantages of doping for introducing oxygen defects into CeO_2 are self-evident. Different doping effects can be achieved by selecting different doped ions and concentrations. However, this method has certain limitations due to the principle that the ion radius and valence state of the doped elements should not differ too much from cerium's.

4.2. Chemical Reduction

As the reaction center of the Mars van krevelan mechanism in the catalytic reaction, oxygen vacancies are generated and consumed cyclically with the redox of Ce^{4+}–Ce^{3+}. In general, the oxidation process of Ce^{3+} is rapid, whereas the reduction of Ce^{4+} is relatively slow. A feasible reduction method to promote the reduction of Ce^{4+} to Ce^{3+} is adopted to contribute the introduction of oxygen vacancies in CeO_2, which is necessary to improve the catalytic activity.

Among the numerous techniques, reducing CeO_2 under CO and H_2 atmospheres as a convenient and efficient technology has

© 2021 Wiley-VCH GmbH

received more interest in the past few decades.[47] Bernardi's group prepared defect-controllable CeO_2 through thermal treatment under a CO atmosphere.[48] Combining the near ambient pressure X-ray photoelectron spectroscopy (NAP-XPS) technique with the in situ XAS technique, it was found that Ce (III) fraction values as high as 0.92 were achieved at relatively low temperatures. Namely, a higher concentration of oxygen vacancies in CeO_2 is obtained, which is efficient for the CO oxidation reaction (**Figure 6**a). In Figure 6b, the time evolution of the Ce^{3+} fraction by XANES spectra was gained during the thermal treatment of the sample exposed to a CO atmosphere. Figure 6c displays the scheme of the vacancy transport model and CeO_2 reduction by the CO atmosphere with the surface vacancy moving toward the region below the surface, where the oxygen moves toward the surface.

Furthermore, Chen' group fabricated defective CeO_2 catalysts by means of annealing at 300 °C in air, vacuum, and H_2 severally. By comparison, they observed that the concentration of oxygen defects in CeO_2 increased more obviously under a H_2 atmosphere compared to other ways. The oxidation state of CeO_2 from Ce^{4+} to Ce^{3+} changed due to the further exposure to H_2, which causes the elimination of oxygen atoms on the surface to produce oxygen vacancies.[49] Different from traditional approaches, Zhang et al. also achieved the purpose of controllably tuning

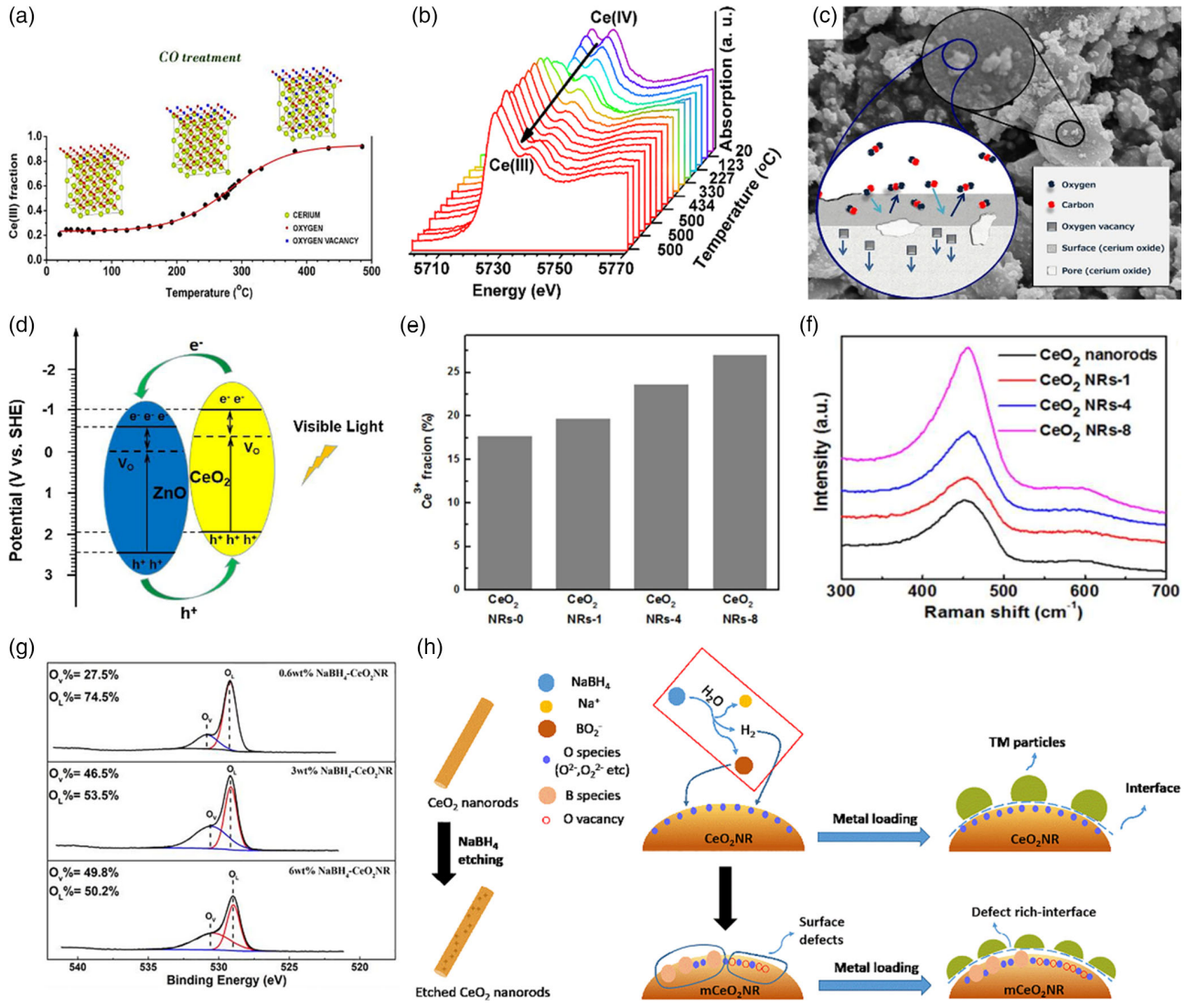


Figure 6. a) The relation between Ce (III) fraction values and reduction temperature (T_R). b) Selected in situ time-resolved XANES spectra of the A70 sample during exposure to a CO atmosphere. c) Schematic representation of the vacancy transport model and the CeO_2 reduction by the CO atmosphere. a–c) Reproduced with permission.[48] Copyright 2017, Elsevier. d) Possible mechanism of charge separation and production of oxidation groups over CeO_2/ZnO photocatalyst under visible light irradiation. Reproduced with permission.[50] Copyright 2020, Elsevier. e) Surface Ce^{3+} fractions of the as-synthesized CeO_2 nanorods and the etched CeO_2 nanorods with 1, 4, and 8 reduction/oxidation cycles, respectively. f) Raman spectra of as-synthesized CeO_2 NRs and the treated CeO_2 NRs with various cycles (1, 4, and 8) of the chemical reduction/oxidation. e,f) Reproduced with permission.[54] Copyright 2015, Royal Society of Chemistry. g) XPS spectra of O 1s for the CeO_2 NR. h) The mechanism of $NaBH_4$ etching on CeO_2 NR and TM-CeO_2 NR catalysts. g,h) Reproduced with permission.[56] Copyright 2020, Wiley-VCH.

© 2021 Wiley-VCH GmbH

the concentration of oxygen defects in CeO_2 through varying the ratio of air:N_2 during calcination. And they emphasized that the rate of carrier migration is attributed to the coordination between oxygen vacancies and the composite semiconductor (CeO_2–ZnO), as shown in Figure 6d.[50] In general, atmosphere treatment is the simplest and most common means to improve the concentration of oxygen defects in CeO_2, but high-temperature treatment may also damage the crystal surface of the sample, so the specific implementation plan needs to be tailored according to the characteristics of different systems.

Apart from the atmosphere reduction treatment, the use of reduction reagents can also achieve similar results.[51] Konsolakis et al. recently summarized the surface structure modification of CeO_2 via accurate fabrication and modification. Among various strategies, chemical etching treatment as a controllable method can modify the surface structure at low temperature, which shows great potential to generate more adsorption and active sites for heterogeneous catalytic reactions.[52] Furthermore, Gao's team treated europium-doped CeO_2 by chemical etching with ascorbic acid and hydrogen peroxide. Due to the reduction of Ce^{4+} to Ce^{3+}, the excitation of Ce^{4+} by O^{2-} was blocked, thus significantly reducing its fluorescence intensity.[53] The specific surface Ce^{3+} fractions associated with great catalytic performance for CO oxidation also continually increased with increasing etching cycles of the reduction/oxidation treatment, as shown in Figure 6e.[54] By the Raman spectra in Figure 6f, the band at about 600 cm^{-1} is ascribed to the intrinsic oxygen vacancies because of the presence of Ce^{3+}.

Except for ascorbic acid, as mentioned previously, sodium borohydride ($NaBH_4$), another strong reducing agent commonly used in industry and laboratories,[55] is also expected to introduce oxygen defects into CeO_2 systems. For instance, Wang's team transformed the surface structure of a CeO_2 NR by etching with $NaBH_4$.[56] The O 1*s* spectra for the CeO_2 NR are displayed in Figure 6g; the peaks at 529.3 and 531.4 eV are ascribed to lattice oxygen and oxygen vacancy on the surface of the CeO_2 NR. They observed that the 6 wt% $NaBH_4$ modified CeO_2 NR showed the highest concentration of oxygen vacancies and the lowest temperature reducibility. In addition, the possible mechanism of $NaBH_4$ etching CeO_2 can be described as shown in Figure 6h; the surface defects that also can act as stable adsorption sites for transition metal oxide result in better diffusion into the CeO_2 NR lattice due to the enrichment of surface defects in the $NaBH_4$-treated CeO_2 NR.

4.3. Size and Morphology Control

With the incredible expansion of nanomaterials in various fields, demonstrating the limitless possibilities of this technology, the trend of manufacturing nanoscale materials is ever-increasing. Indeed, nanomaterials with large surface area to volume ratios and changes in lattice parameters enable CeO_2 to change the lattice parameter, which is related to the lattice strain caused by the induction of Ce^{3+}.[47a,57] It is verified by Deshpande et al. that the concentration of Ce^{3+} and oxygen vacancies increases with the decreasing size of nanoceria due to higher oxygen vacancies in the smaller particles. The larger lattice strain led by Ce^{3+} ions further impacts the lattice parameter of the particles, as shown in **Figure 7**a.[57] Neyman and co-workers measured the concentration of oxygen vacancies and found that particle size in the range of 2–4 nm compared to extended surfaces greatly promotes the removal of oxygen, and the vacancy formation energy also reaches a minimum value (Figure 7b).[58] Moreover, other studies emphasized and indicated that the oxygen defect formation energy (E_f) of nanosized CeO_2 is significantly lower than that of the bulk structure, which dramatically enables the higher reactivity of nanoparticles to be achieved at lower temperatures.[59] These examples well demonstrate that by controlling the size of CeO_2 nanometer particles, its specific activity can be possibly regulated.

With the deepening of research on CeO_2, there also has been increased attention in altering the morphology as an equally important factor in producing oxygen defects. Numerous studies have concentrated on the correlation between the exposed crystal plane and morphological control of CeO_2 and surface defects.[13,60] There are differences in the energy of formulating oxygen defects on different crystal planes. Consequently, the crystal planes with low oxygen defect formation energy are exposed on precisely controlling the morphology, which can also introduce more oxygen defects, which is of great significant implication to optimize the conversion of Ce^{4+} to Ce^{3+} and improve the oxygen storage capacity.[61] Mai et al. synthesized single-crystalline and uniform CeO_2 nanomaterials with different morphologies of nanopolyhedra, nanorods, and nanocubes. They demonstrated that the exposed surfaces composed of the (100)/(110) plane with rods and cubes were more active to CO oxidation and exhibited higher surface oxygen storage capacity than the polyhedral (111) plane surface material.[60a] To the best of our knowledge, the high oxygen storage capacity of CeO_2 is attributed to the rich surface oxygen defect density. Lei et al.[62] and Si and Flytzani-Stephanopoulos[63] also confirmed this view; due to the smallest oxygen defect formation energy of the (110) crystal plane, the sample with more exposure to the (110) crystal plane has the maximum oxygen defect concentration value and thus shows significant reactivity and catalytic applications. Both theoretical calculations and practical experiments show that the (110) crystal plane of CeO_2 has a lower oxygen defect formation energy compared with the (100) and (111) crystal planes. Therefore, controlling the synthesis of CeO_2 nanomaterials with more (110) crystal plane is beneficial to increasing the oxygen defect concentration.

However, a result is different from those of the past. Amoresi et al.'s research held that the concentration of oxygen vacancies evaluated by the Raman scattering spectra demonstrated that bean-type CeO_2 presents (111) and (200) orientations that are in the maximum value as high as 9.9, which seems to be paradoxical to the previous viewpoint considering that the (110) crystal plane has the maximum oxygen defect concentration value. As shown in Figure 7d–g, they also simulated several kinds of CeO_2 planes and the surface stability order, calculated exploiting the equation of surface energy according to DFT, can be specifically arranged as (111) < (110) = (220) < (311) < (100) = (200).[13] The (111) crystal plane has the lowest defect formation energy; however, it possesses a lower defect concentration than the (110) crystal plane. Aiming at the issue, several investigations related to the adsorption and dissociation of various probe molecules such as CO, methanol, and formic acid have been increasingly concerned

© 2021 Wiley-VCH GmbH

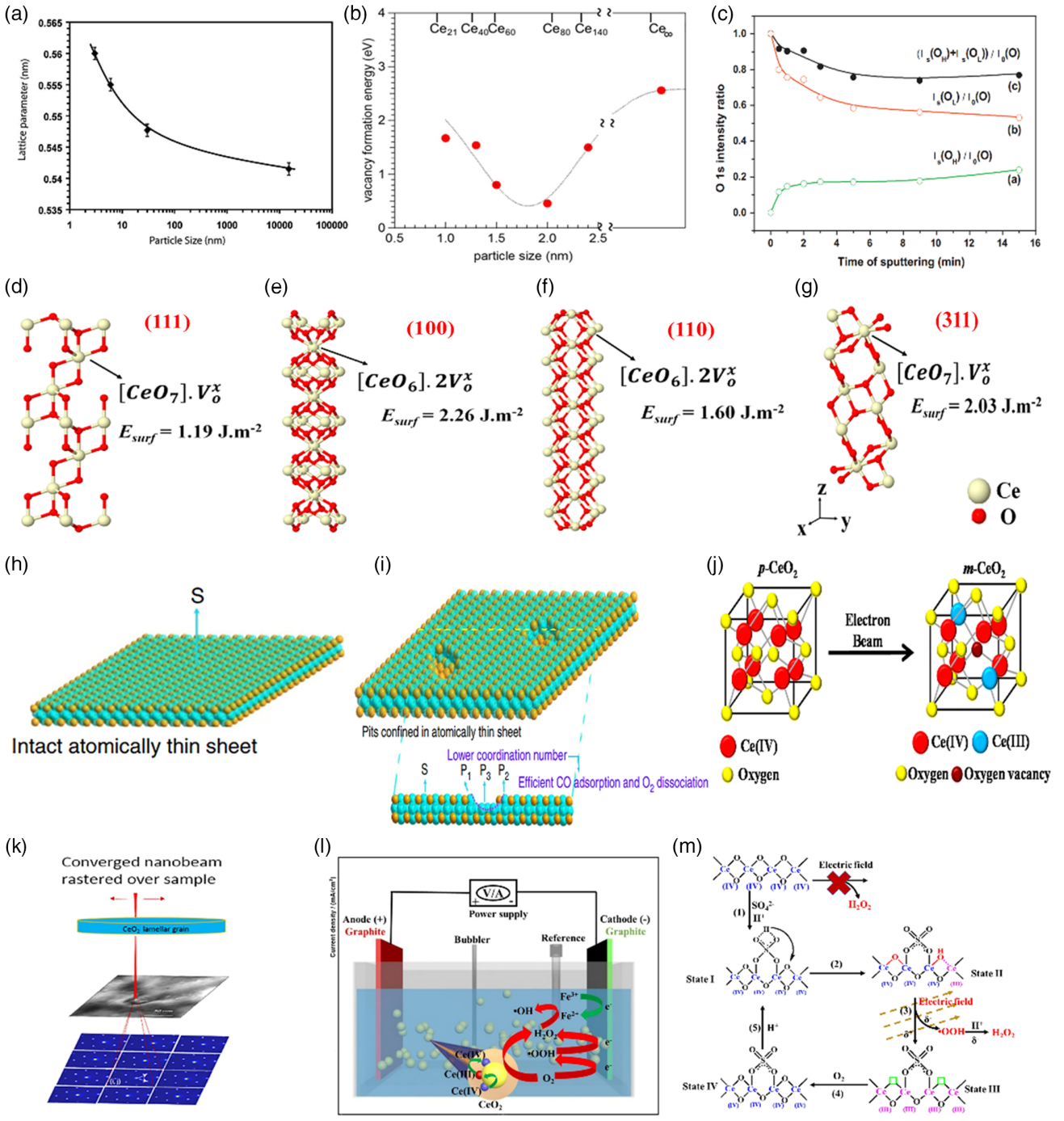


Figure 7. a) Semilog plot of the lattice parameter as a function of the particle size. Reproduced with permission.[57] Copyright 2005, American Institute of Physics. b) Size dependence of vacancy formation energy for different ceria nanoparticles. Reproduced with permission.[61c] Copyright 2017, American Chemical Society. c) Intensity ratios between the two O species (O_H and O_L) and that of the initial O 1s peak as a function of sputtering time: a) I_s (O_H)/I_0 (O), b) I_s (O_L)/I_0 (O), and c) I_s (O_H) + I_s (O_L)/I_0 (O). The symbols I_s (O_H), I_s (O_L), and I_0 (O) stand for the intensities of the high-binding-energy O 1s peak at 531.8 eV, the low-binding-energy O 1s peak (lattice oxygen in CeO_2), and the initial O 1s peak of CeO_2, respectively. Reproduced with permission.[69] Copyright 2012, Elsevier. The surface models for each morphology of the CeO_2 nanocrystals are shown for d) (111), e) (100), f) (110), and g) (311) surfaces. d–g) Reproduced with permission.[13] Copyright 2019, American Chemical Society. h) Intact thin CeO_2 sheets. i) Schematic illustration for evaluating catalysis location and activity. Atomically thin CeO_2 sheets with surface-confined pits, P_1 and P_2, stand for the representative pit-surrounding surface Ce sites, while P_3 represents the bottom Ce site of the pit; "S" stands for the surface Ce site of the atomically thin sheet and around the defects of the bulk material h,i) Reproduced with permission.[64] Copyright 2013, Springer Nature. j) Schematic model illustrating the change in crystalline structure of CeO_2 due to the formation of Ce (III) and oxygen vacancy after electron beam irradiation. Reproduced with permission.[71] Copyright 2014, American Chemical Society. k) Schematic illustration of the 4D STEM geometry. Reproduced with permission.[70e] Copyright 2020, Elsevier. l) Device and mechanism diagram. m) Proposed mechanisms in the CeO_2 E-Fenton system. l,m) Reproduced with permission.[72] Copyright 2018, Elsevier.

© 2021 Wiley-VCH GmbH

with growing CeO_2 (111), (100), and (110) planes. Therefore, regulating the exposure of crystal planes needs to be considered according to the specific reaction. Different from the traditional methods mentioned earlier, Sun et al.[64] manufactured thin CeO_2 sheets with lower coordination numbers and artificial pits through a simple annealing process, as shown in Figure 7h,i. They found that the ultrathin CeO_2 nanosheets have a higher oxygen defect concentration compared with the bulk-phase CeO_2, which is not only due to reduced Ce—O coordination numbers, but also fostered by tuning many pits into the nanosheets.

4.4. Other Methods

In addition, with the vigorous development of material science, Ar^+ bombardment and X-ray irradiation that lead to obvious changes in CeO_2 of valence state, structure, or position are regarded as modern methods to introduce defects. For instance, Paparazzo studied that CeO_2 is partially reduced to Ce^{3+} oxidic species via prolonged Al Kα irradiation.[65] A similar study by Rao and Shripathi treated CeO_2 samples with Al Kα X-rays and found that the color of cerium dioxide changed significantly after exposure to X-rays.[66] Moreover, Qiu et al. compared the reduction ability of nanocrystalline and micron-crystal CeO_2 by X-ray and Ar^+ bombing and concluded that nanocrystalline CeO_2 has a higher reduction degree than micron-crystal CeO_2 under the same conditions due to its higher oxygen atom diffusion characteristics.[67] Previously, Holgado et al. studied CeO_2 films bombarded with Ar^+ at 25 °C, and XPS analysis showed that the CeO_2 after treatment was mainly converted into Ce_2O_3. Then, the CeO_2 thin film was oxidized deeply with oxygen and the existence of stable Ce^{3+} on the surface of the sample was found.[68] In addition, Wang et al. found that the formation of oxygen vacancies on the surface of CeO_2 was induced by Ar^+ bombardment that caused oxygen atoms to be preferentially removed from the surface, and the reduction rate was relevant to the energy and amount of Ar^+ exposed on the CeO_2 surface. Figure 7c shows the total intensity of O_L and O_H only remains at ≈80% of the initial O 1*s* intensity of CeO_2 after 15 min sputtering, which also confirms the aforementioned opinion.[69]

There have been many recent reports on an electron beam that can be effectively utilized to introduce defects.[36,70] Khan et al. reported an electron beam irradiation (30 and 90 kGy) method (Figure 7j) to initially narrow the bandgap of CeO_2 through creating sorts of defects. The defect concentration is higher than that of CeO_2 in the bulk phase.[71] Ding et al. also created a gradient in oxygen vacancy concentration: a small region (≈30 nm in diameter) inside a ceria grain is reduced to the C-type $CeO_{1.68}$ phase using the ionization or radiolysis effect of a high-energy electron beam (Figure 7k).[70e] Furthermore, as an effective approach, electric field induction was successfully applied in the reinforcement of the CeO_2 catalytic performance. For example, Ren and co-workers designed an E-Fenton system by means of electric field induction to get the utmost out of the oxygen storage capacity of CeO_2, as described in Figure 7l. XRD analysis shows the presence of oxygen-deficient CeO_2 and the van der Waals gap in the oxygen-deficient CeO_2 is on an expanding trend. The reversible conversion of cerium between two stable states (Ce^{4+} and Ce^{3+}), lattice oxygen to surface oxygen, is conducive to the formation of H_2O_2 in the electric field to accelerate the degradation of waste water as shown in Figure 7m.[72]

Undoubtedly, these results provide researchers with a wide variety of options to introduce oxygen defects into CeO_2, different approaches having their own advantages and disadvantages as shown in **Table 2**. In the practical application, the specific selection method depends on the targets for catalytic reactions.

5. Applications

As discussed previously, defective CeO_2 catalysts are technologically important functional materials in many applications. In the following sections, a few typical examples regarding defective-CeO_2-based catalysts are selectively reviewed.

5.1. Small-Molecule Oxidation Reaction

5.1.1. CO Oxidation

The carbon monoxide (CO) catalytic oxidation reaction has been widely used in modern life and attracted widespread attention, for example, in CO sensors, water–gas shift, and automobile exhaust purification. At present, the Mars van Krevelen mechanism is widely recognized by researchers.[73] The CO molecules react with the lattice oxygen of the oxide to generate CO_2 and oxygen vacancies on the surface of CeO_2, and the O_2 molecules fill the oxygen vacancies to complete the cycle (**Figure 8**a). Hence, oxygen vacancy or Ce^{3+} plays an important role in this process. For instance, Xie and his team designed CuO/CeO_2 with different facets and applied preferential CO oxidation, and observed that the catalysts exposed to (111) and (002) crystal planes in the synthesized samples showed lower CO conversion temperatures and higher oxygen vacancy concentration than those exposed to other crystal planes (Figure 8b,c). Combined with DFT calculations, the excellent catalytic activity was attributed

Table 2. A comparable summary of different strategies for introducing defects.

Strategies for introducing defects	Advantages	Disadvantages
Metal doping	Doping can change the geometrical and electronic structure of CeO_2, with strong controllability.	The ion radius and valence state of the doped element and cerium should not differ too much.
Chemical reduction	Simple, universal, and efficient.	The high temperature associated with the process is destructive to the morphology of the sample.
Size and morphology control	Low defect generation energy can be obtained by controlling the formation of different crystal planes.	Uncontrollable defect concentration.
Ar^+ bombardment, X-ray irradiation, and electron beam irradiation	Convenient, controlled synthesis by controlling the radiation or bombardment intensity.	The large physical bombardment effect results in poor stability. Harsh treatment conditions.

© 2021 Wiley-VCH GmbH

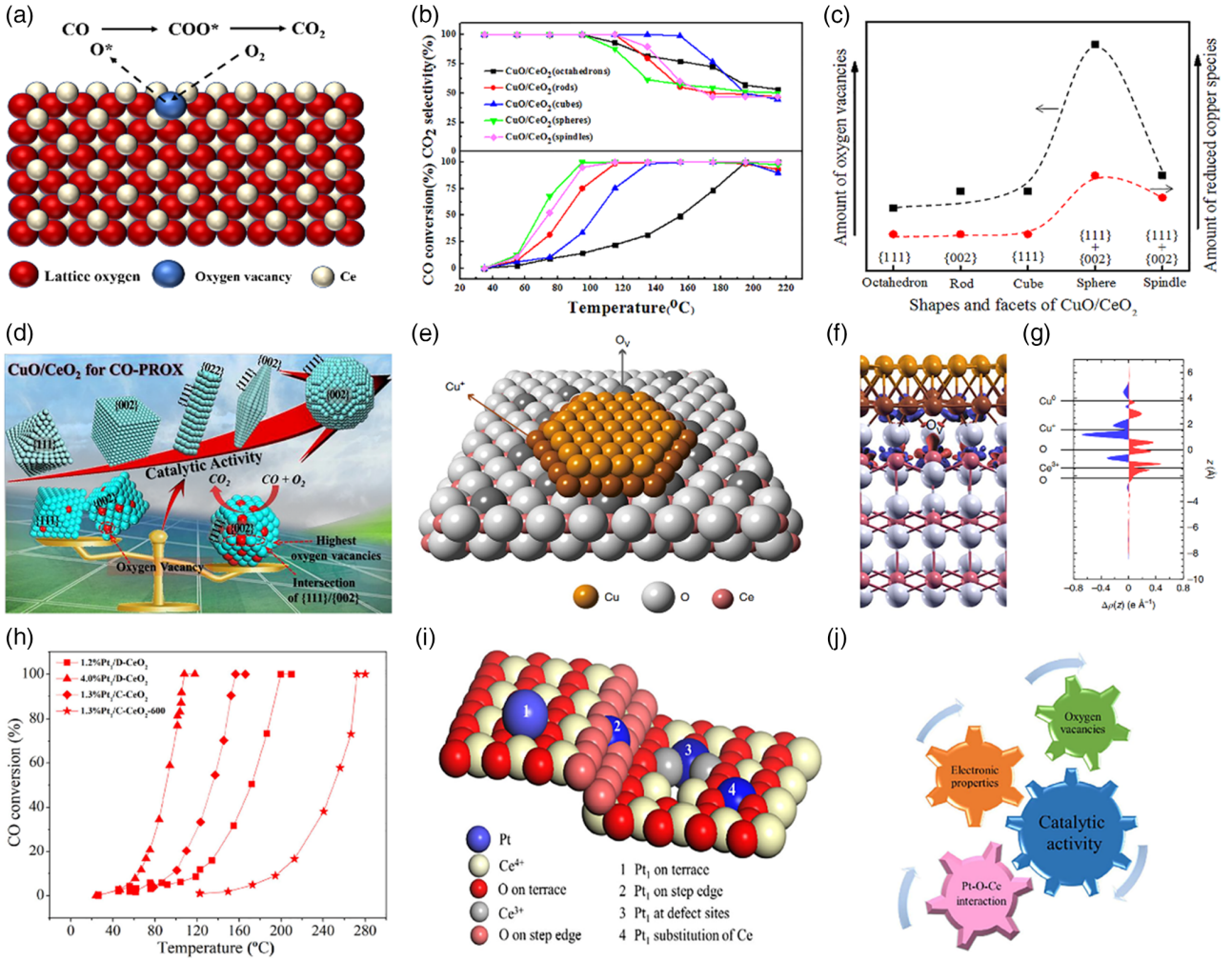


Figure 8. a) Schematic of the catalytic reaction of CO oxidization by CeO_2. b) CO conversion and CO_2 selectivity over the CuO/CeO_2 catalysts with different support shapes. c) Plots of the amount of oxygen vacancies and reduced copper species for the CuO/CeO_2 catalysts with different support shapes. d) Possible mechanism of CO catalytic oxidation by CuO/CeO_2. a–d) Reproduced with permission.[74] Copyright 2018, Elsevier. e) A schematic illustration of the typical Cu bilayer on ceria. f) Calculated equilibrium structure and charge transfer between the Cu bilayer and the reduced ceria surface in a periodic supercell. g) Plane-integrated bonding charge $\Delta\rho$ (z) as a function of position across the copper–ceria interface. The red and blue areas represent charge accumulation and depletion, respectively. e–g) Reproduced with permission.[76] Copyright 2019, Springer Nature. h) Scheme model of CeO_2-supported Pt single atoms with different local coordination structures. i) Catalytic performance of Pt_1/CeO_2 single-atom catalyst water-mediated CO oxidation. j) The correlation among surface defects, metal loading, electronic properties, and Pt—O—Ce bonds. h–j) Reproduced with permission.[7b] Copyright 2019, Springer Nature.

to the formation of Cu^{2+} induced by the high concentration of oxygen vacancies in CeO_2, as shown in Figure 8d.[74]

Moreover, oxygen defects can also provide stable adhesion points for metals, facilitate the recombination of active metals and CeO_2 carriers, accelerate electron transfer and interaction, and further improve the catalytic oxidation activity of CO.[75] Chen et al. simulated the two-layer atomic structure of Cu/CeO_2 based on the spectral analysis results as shown in Figure 8e. The experimental and theoretical calculation results show that at the defect location, the surface of the reduced CeO_2 offers more adhesion sites for Cu^+, and this strong binding inhibits the separation of Cu clusters and maintains the stability of the two-layer structure. The large distortion of the plane structure is further evidence of the strong interaction, as shown in Figure 8f. Figure 8g shows the strong chemical bond between the two-layer Cu atom and the reduced CeO_2 due to the frequent charge transfer.[76] To reinforce this interaction, other researchers have introduced highly reactive noble metals such as Au, Pd, and Pt. Ye et al. focused their research on how to stabilize the Pt atom, which is important for the electron interaction at the Pt–O–Ce interface (Figure 8h).[7b] In the water-mediated CO oxidation, when the doping amount of Pt is 4%, T_{50} (the reaction temperature required for 50% CO conversion) is lower than that of other samples under the same conditions (Figure 8i). They also summarized the correlation among surface defects, metal loading, electronic properties, and Pt—O—Ce bonds (Figure 8j). This is a great

© 2021 Wiley-VCH GmbH

contribution to improve the knowledge system of oxygen defect–electronic structure–catalytic activity. Furthermore, Ke et al. explored the influence of the local coordination structure of Pt/CeO_2 on its catalytic activity of CO oxidation. Kinetic results show that the reaction rate is independent of the partial pressures of CO and O_2, which fits perfectly with the Mars van Krevelen mechanism.[77] From the aforementioned, oxygen defects are the key factor in the catalytic oxidation of CO, and their main functions include adsorption and activation of O_2, stabilization of metals loaded on the surface of CeO_2, and enhancement of electron interactions.

5.1.2. Methanol Oxidation

Considering the ever-increasing energy scarcity and environmental pollution, researchers have paid more attention to some molecule oxide batteries to obtain clean energy. Methanol oxidation, as a kind of convenient and high-energy-density reaction, has a great application prospect in fuel cells.[78] However, it is limited by the high-cost noble metal catalyst, so a great deal of interest has gradually turned to the lower cost of metal oxides. CeO_2 with high oxygen storage capacity and abundant oxygen defects has been extensively investigated.[79] Recently, Jiang et al. constructed a stable Pt–O–Ce interface generated by strong metal–carrier interaction to investigate methanol oxidation. They found that Pt atoms are stabilized on the CeO_2 surface due to the large number of attachment points provided by oxygen vacancies, which leads to the distorted Pt–O–Ce interface. This deformation of the Pt–O–Ce interface not only adjusts the Fermi energy level and electron density between Pt and CeO_2 to balance and achieves optimized electronic structure, but also promotes methanol and O_2 adsorbtion on the interface for efficient catalysis.[80] As shown in **Figure 9**a, methanol is activated to form methoxy species, which then reacts with O and surface hydroxyl groups to form metallic organic molecules at the Pt–O–Ce interface, and finally is oxidized to CO_2 and H_2O. In another work by Liu and his team, microwave-assisted polyol reduction was used to fabricate $PtCu/CeO_2$/CNTs (Figure 9b). They found that the oxygen vacancy effect on CeO_2 not only plays an important role in achieving efficient charge transfer in methanol oxidation reaction, but also enhances the electrical conductivity of the catalyst.[81] In short, defective CeO_2 possesses full potential in methanol oxidation. However, the catalytic activity of the single defective CeO_2 catalyst is relatively low and the current understanding of the role of oxygen defects in methanol oxidation is still relatively weak. Therefore, defective CeO_2 still needs to be thoroughly studied.

5.2. Small-Molecule Reduction Reaction

In recent years, the CO_2 reduction reaction (CO_2RR) and N_2 reduction reaction (NRR) have been widely used in converting CO_2 and N_2 into high-value-added chemicals.[82] Noble metals, including Pt, Pd, Rh, and Au, were considered as the most promising materials for the CO_2RR and NRR. But their large-scale application is limited by their high price. Therefore, it is urgent to explore low-cost and efficient catalysts to replace the function of noble metals in the CO_2RR and NRR. In the past decades, CeO_2 with an oxygen defect structure could help to produce stronger metal–carrier interactions and improve metal dispersion. It has gradually been regarded as an ideal substitute for noble metals.

5.2.1. CO2 Reduction

The CO_2RR has become a continuous research hotspot in energy- and material-related fields. CO_2 molecules can be converted into high-value-added chemicals via chemical transformation, biological transformation, photocatalytic reduction, and electrocatalytic reduction processes. Recently, Wang et al. constructed the system of single-atomic Cu with multiple oxygen vacancies on CeO_2 and applied it to the electrocatalytic reduction of CO_2 to produce CH_4. They simulated the surface microstructure of the synthesized sample via combining theoretical calculations. Structure models with different oxygn vacancies are as shown in Figure 9c–g, where each highly dispersed Cu atom is stably attached to the oxygen vacancy (V_o) on the (110) surface of CeO_2. The formation energy of 3 V_o on pure CeO_2 (110) is specified to be 1.65 eV, explaining that the single-atomic Cu site is the most stable on CeO_2 with the 3 V_o bound structure. Moreover, the structural characterization results also further confirmed that the catalyst not only has a low coordination number, but also reaches the full potential in the CO_2RR, and the Faraday efficiency can reach 58% (Figure 9h).[8c] Zong focused on the geometric and electronic effect at the Cu/CeO_x@CNFs. According to the electrochemical active area shown in Figure 9i, it is revealed that more CO_2 could be adsorbed when oxygen defects act as the active sites.[82a] Except for these CO_2RRs that were reduced to CH_4, there have also been many studies on CO_2RR to formic acid (COOH),[83] ethanol (C_2H_5OH),[84] CO,[45,85] and other chemicals. For example, Verlto and his team successfully deposited CeO_2 on boron-doped polycrystalline diamond cathodes by the electrochemical precipitation method. The test results showed that it reduced CO_2 to formic acid at an overpotential of less than 50 mV, with a Faraday efficiency of 40%.[86] In another work, the high oxygen vacancy concentration of the heterojunction is the key to improving the selectivity and activity of CO_2 reduction to formic acid, which makes the Faraday efficiency as high as possible, 76.4% at 0.75 V versus RHE (-6.1 mA cm^{-2}) as shown in Figure 9j.[83] At present, in addition to the properties, others have paid attention to the pathway of CO_2 reduction as shown in **Figure 10**a. They have calculated and simulated the process of CO_2 reduction through density functional theory, and described in detail the role played by metals such as Pt, as well as the specific energy required for the adsorption of CO_2 to the catalyst.[87] There are still many problems to be solved for large-scale practical application of the CO_2RR, including improving the conversion efficiency and current density, reducing the overpotential, and improving the selectivity. Therefore, the key issues such as the optimization of the related materials and the research of the catalytic mechanism need to be further explored.

In addition to electrocatalysis, photocatalytic CO_2 reduction as a green and efficient pathway has also attracted widespread attention.[8a,8b,88] Using SiO_2 as a template, Liang and his team prepared a hollow heterostructure with abundant oxygen vacancies, the g-C_3N_4@CeO_2 photocatalyst. They clearly pointed out the role of such a hollow structure and oxygen vacancies in

© 2021 Wiley-VCH GmbH

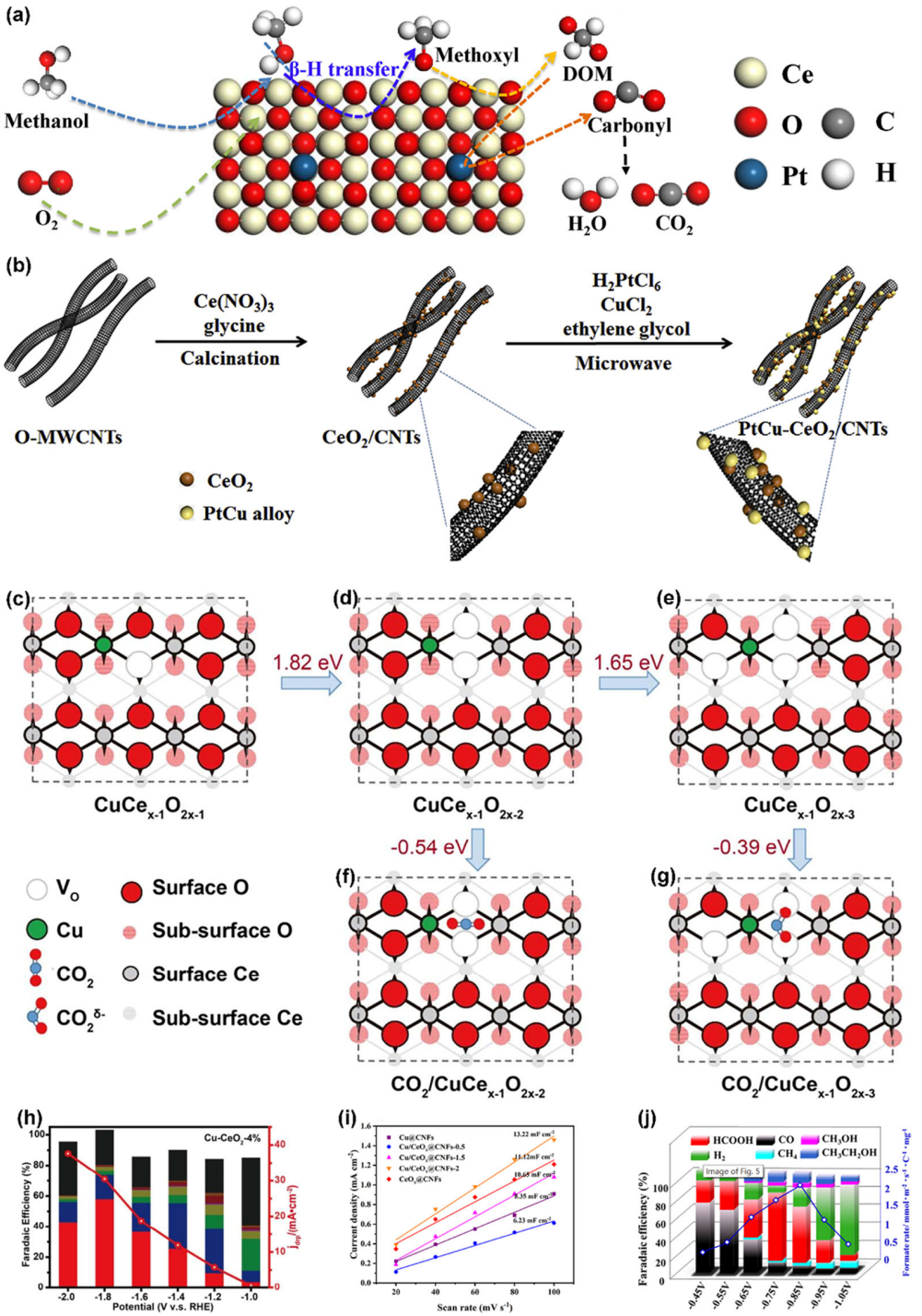


Figure 9. a) The proposed oxidation mechanism for methanol oxidation over Pt_1–CeO_2 (100) catalyst. Reproduced with permission.[80] Copyright 2020, Elsevier. b) The synthesis procedure of Pt Cu–CeO_2/CNT samples with different Pt-to-Cu ratios. Reproduced with permission.[81] Copyright 2020, Elsevier. Structure models of CeO_2 (110) doped with one single Cu site, with c) 1 oxygen vacancy (V_o), d) 2 V_o, and e) 3 V_o. f,g) Structure models of these V_o-bound, single-atomic Cu sites on CeO_2 for CO_2 adsorption and activation. h) Faradaic efficiencies (bars, left *y*-axis) and deep reduction product current density (red curves, right *y*-axis) of Cu–CeO_2-4%. c–h) Reproduced with permission.[8c] Copyright 2018, American Chemical Society. i) Electric double-layer capacitance. Reproduced with permission.[82a] Copyright 2020, Elsevier. j) Applied electrolysis potential dependence of normalized rate (right axis) and Faradaic efficiency (left axis) for formate on Co_3O_4–CeO_2/low graphitic carbon. Reproduced with permission.[83] Copyright 2019, Elsevier.

© 2021 Wiley-VCH GmbH

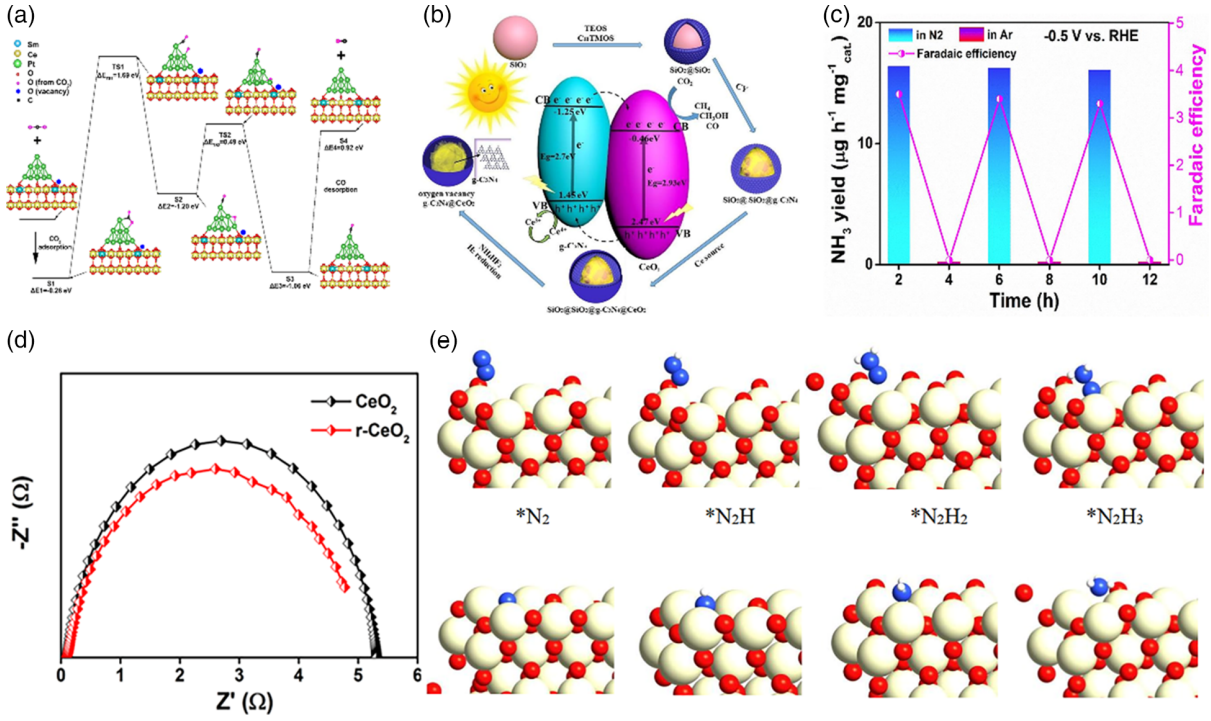


Figure 10. a) Pathway of CO_2 reduction at the Pt_{upper} site on the Pt_{10}/samaria-doped ceria–3VAC (vacancy)–V surface. Reproduced with permission.[87] Copyright 2019, American Chemical Society. b) Representative illustration of the assembling of g-C_3N_4@CeO_2 hollow heterostructures and machanism for photocatalytic CO_2 reduction. Reproduced with permission.[88a] Copyright 2019, Elsevier. c) The NH_3 production rates (left *y*-axis) and FE NH_3 (right *y*-axis) of r-CeO_2 at −0.5 V versus RHE. d) Nyquist plots of CeO_2/CP and r-CeO_2/CP. c,d) Reproduced with permission.[93] Copyright 2019, American Chemical Society. e) The optimized CeO_2 (111) surface structures with an oxygen vacancy along the NRR reaction path for N_2 conversion to NH_3 (Ce: shallow yellow sphere; O: red sphere; N: blue sphere; H: white sphere). Reproduced with permission.[94] Copyright 2019, Wiley-VCH.

enhancing the charge separation efficiency and interfacial charge transfer (Figure 10b).[88a] At the same time, the synergistic effect of heterostructures is also an important factor for the high CO_2RR. Moreover, the addition of oxygen vacancies can also improve the chemical adsorption ability of oxygen on the CeO_2 catalyst surface, and the adsorbed oxygen species play a crucial role in capturing more electrons to form surface oxygen-free radicals and further promoting the photocatalytic conversion of CO_2.

5.2.2. N_2 Reduction

The activation and reduction of N_2, as one of the most challenging topics, have been explored for several decades.[89] However, the required reaction conditions, such as high temperature and high pressure, are relatively extreme.[90] Therefore, reseachers have been looking forward to finding an effective nitrogen fixation method to reduce N_2 to NH_3 under mild conditions to alleviate the negative impact of ammonia synthesis on the environment. Electrochemical N_2 reduction has been widely studied because it is green and eco-friendly, and various kinds of electrocatalysts have been developed.[91] In many reports on the reduction of N_2, oxygen vacancies can weaken the N_2 triple bond by effectively trapping electrons on the antibonding orbital of the adsorbed N_2, which is conducive to the activation and reduction of N_2.[90,92] This enables us to further clarify the direction of electrocatalyst optimization, such as increasing the oxygen vacancy concentration of the catalyst and strengthening electron transfer. Based on this, CeO_2 with a defective structure provides a better choice and is generally accepted. For instance, Xu et al. proved that CeO_2 nanorods with oxygen vacancies have excellent selectivity and stability in the NRR. As the overpotential of the reversible hydrogen electrode is 0.5 V, the yield of NH_3 can be reached to 16.4 $\mu g\,h^{-1}\,mg^{-1}_{cat}$ (Figure 10c). In combination with EIS analysis (Figure 10d), they also found that CeO_2 nanorods with a faster NRR reaction rate had lower charge transfer resistance, indicating that oxygen vacancies can boost the NRR.[93] However, how the oxygen vacancy interact at the N_2–CeO_2 interface is still a problem. Liu et al. proposed a model, as shown in Figure 10e, and described how N_2 gets released as NH_3 by the action of oxygen vacancies.[94] It is helpful for designing defective-CeO_2-based efficient catalysts and further understanding the mechanism of CeO_2 in N_2 reduction.

5.3. Water Splitting

Along with the depletion of non-renewable resources such as fossil fuels and the increasingly serious environmental pollution, a crowd of attention has been turned on the clean energy such as hydrogen. Electrochemical water splitting is one of the most economical and clean hydrogen production strategies, which

© 2021 Wiley-VCH GmbH

contains two half-cell reactions: 1) the reduction process at the cathode is the hydrogen evolution reaction (HER) and 2) the oxidation process at the anode is the oxygen evolution reaction (OER).[68] However, these reactions still encounter slow reaction kinetics, so the development of low-cost, efficient, and green electrocatalysts has become the key to solving the current energy problems.[95] Fortunately, CeO_2 as a cheap catalytic material has been widely used in water splitting because of its oxygen-rich defects through the conversion between Ce^{4+} and Ce^{3+}.[9b,96] Therefore, we summarized recent advances of defective-CeO_2-based catalysts for water splitting attempting to explore how oxygen vacancies act on the electrode and enhance the performance of water splitting.

5.3.1. OER

The OER is a four-electron reaction with slow reaction kinetics, which has limited the efficiency of water splitting.[97] The unique defect structure of CeO_2 provides a stronger adsorption site, which enables it to improve oxygen mobility. Some studies have shown that CeO_2 as a carrier may be beneficial to the formation of OH_{ad} because the abundant oxygen vacancies in CeO_2 could reinforce the bind adsorbates.[98] Xia and his team developed a system that treats CeO_2 as support for a nickel–iron–chromium hydroxide (NFC), which displayed a lower overpotential at 10 mA cm^{-2} of 230.8 mV and a Tafel slope of 32.7 mV dec^{-1}. They also studied the role of CeO_2 in the system. As shown in **Figure 11**a, the maximum energy barrier of the reaction pathway with the addition of CeO_2 is significantly lower than that of the NFC system alone. Also, they proposed that the CeO_2 layer facilitates the OER process by forming a "*d–f* electron ladder" that acts as a charge transfer channel, as shown in Figure 11b.[99] Yu and his team synthesized high-valence Ni-doped CeO_2 covered with FeOOH nanosheets in one step. The interesting thing is its catalytic reaction process: Fe^{3+} is hydrolyzed and Ni^{2+} is replaced, and the Ni^{2+} in the substitution reaction is oxidized to Ni^{3+}/Ni^{4+} by Ce^{3+} and abundant oxygen vacancies. The final catalyst showed a lower overpotential (195 mV cm^{-1} at 100 mA cm^{-2} current density) in the OER.[100] Constructing a heterostructure is also an effective strategy to promote the OER activity.[9b,101] Taking CoP as an example, in Li et al.'s works, they clarified that such a heterogeneous surface can not only introduce a large number of oxygen vacancies and more catalytic active sites, but also accelerate the interfacial electronic structure and charge transfer, thus decreasing the overpotential, as shown in Figure 11c.[101] As described previously, although CeO_2 itself has poor electrical conductivity, it can be combined with other conductive materials to solve this problem, and its abundant oxygen deficiencies have attracted many researchers to apply it in overall water splitting.

5.3.2. HER

The introduction of oxygen vacancies overcomes the problems that pure CeO_2 usually has poor electrical conductivity and a high hydrogen adsorption/desorption barrier.[102] Moreover, the defective CeO_2 has strong electronic interaction with the composite material.[103] Therefore, recently, researchers have attempted to regulate the crystallinity and electronic properties of catalysts by introducing complexes into the defective CeO_2 system, including nitrides,[96,104] phosphides,[9b,101] hydroxides,[105] metals,[106] and alloys.[107] Yao

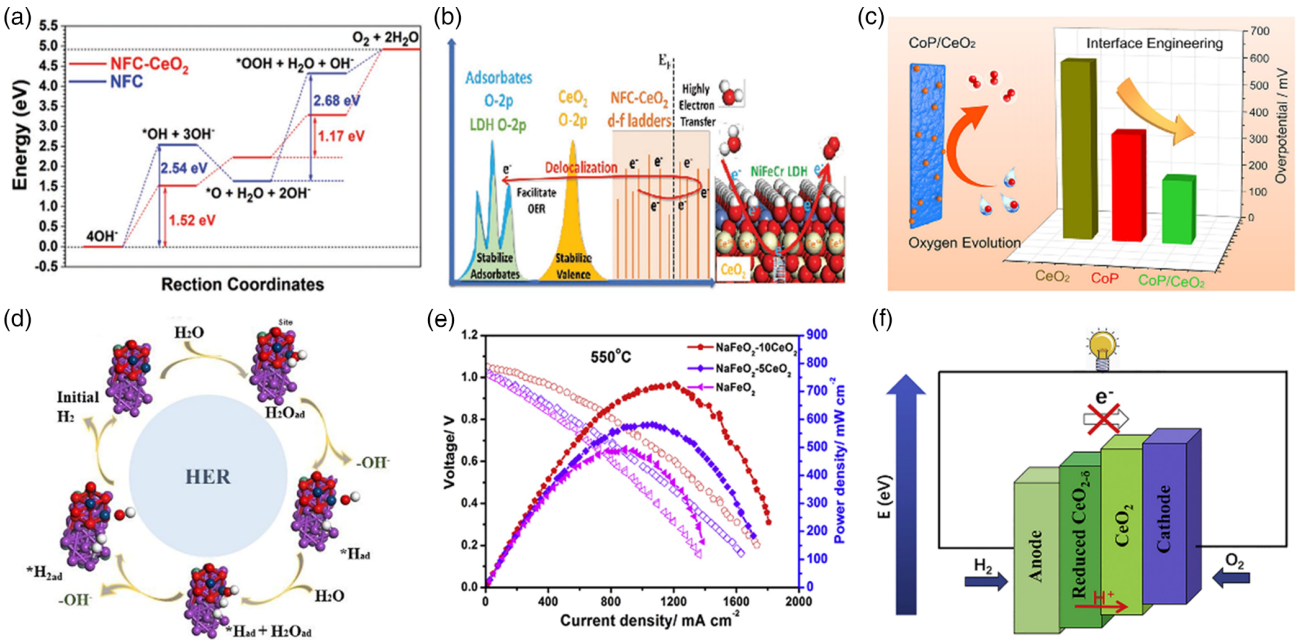


Figure 11. a) Energy pathway of OER on NFC and NFC–CeO_2. b) Schematic diagram of the *d–f* electronic ladders by NFC–CeO_2 for boosting the OER. a,b) Reproduced with permission.[99a] Copyright 2020, Wiley-VCH. c) Effect of interface engineering on overpotential. Reproduced with permission.[101a] Copyright 2020, Elsevier. d) HER cycle mechanism diagram. Reproduced with permission.[104a] Copyright 2020, Elsevier. e) *I–V* and *I–P* curves of $NaFeO_2$–$10CeO_2$ fuel cell at different operating temperatures. Reproduced with permission.[110] Copyright 2021, Elsevier. f) Mechanism of the ionic transportation in CeO_2 nanocube SOFCs. Reproduced with permission.[112] Copyright 2018, Elsevier.

© 2021 Wiley-VCH GmbH

et al. developed a high-performance CeO_2/Co_4N electrocatalyst for electrochemical hydrogen evolution, which enhanced the alkaline HER kinetics and long-term stability (as shown in Figure 11d, the cyclic diagram). They also investigated the role of abundant oxygen vacancies by DFT calculations and experimental results.[104a] The abundance of oxygen vacancies in CeO_2 promotes the adsorption/disintegration ability of water, and the electron transfer between CeO_2 and Co_4N causes the lowest hydrogen adsorption free energy with an overpotential of 30 mV at 10 mA cm^2 in 1.0 M KOH. Krishnan used Al_2O_3 to load CeO_2 in a Ni–P electrode and found that both the increase in the oxygen vacancy concentration and the porosity of the electrode material can be attributed to the higher Ce^{3+} stoichiometric ratio.[108] Their research puts forward that the long-term stability is due to the introduction of the dopant changed CeO_2 lattice parameter, and on the basis of previous studies that oxygen vacancies can change the crystal lattice parameters,[47a,57] we put forward a kind of imagination that the introduction of dopant CeO_2 could gain more oxygen vacancies, thus affecting the lattice parameters and forming a solid solution, so as to achieve long-term stability. Furthermore, the work of Sun et al. constructed a superhydrophilic Ni–Co nanoparticle array coupled with CeO_2 that showed significant durability in alkaline media; the overpotential is 34 mV at 10 mA cm^{-2} and 140 mV at 500 mA cm^{-2}. The superhydrophilic self-supporting electrode structure and interfacial synergies promote water dissociation and optimize the hydrogen binding energy.[107]

5.4. Solid Oxide Fuel Cells (SOFCs)

SOFCs are a kind of all-solid-state energy conversion technology, which is widely concerned in energy utilization. It can convert fuel chemical energy directly into electric energy through electrochemical redox reaction. It possesses the advantages of high-power-generation efficiency, environmental friendliness, wide fuel adaptability, and high-temperature waste heat recovery, and has gradually become an important part of the world energy composition. It is reported that a CeO_2 semiconductor with resistance to carbon deposition can provide fuel for the anode. Some studies have focused on the preparation of coatings to improve the charge separation.[109] For instance, Xing et al. developed a novel composite oxide material for the electrolyte membrane of fuel cells, which was coated with CeO_2 to form a core–shell structure $NaFeO_2$–$10CeO_2$. The ultimate fuel cell efficiency could be up to 727 mW cm^{-2} maximum power output at 550 °C, as shown in Figure 11e. The experimental results show that the CeO_2 shell produces more oxygen vacancies, accelerates proton transfer, and increases the grain boundary conductivity of superoxide radicals.[110] Furthermore, many other reports have been devoted to constructing heterojunction complexes and doping a metal to realize the low-temperature operation of SOFCs.[111] In another work, Li et al. discussed the electrical properties of CeO_2 nanocubes in SOFCs, and found that CeO_2/CeO_{2-x} can offer a high ion conduction path for electrolytes in SOFCs. In Figure 11f, CeO_2 and CeO_{2-x} semiconductors realized efficient charge separation. This is due to the difference of the energy band between the two semiconductors, which forms a double-layer structure to prevent electrons from passing through the device and avoid short circuit of the device.[112]

5.5. Photocatalysis

As an n-type semiconductor with unique physical and chemical properties, CeO_2 has also been widely studied in the field of photocatalysis.[10a,113] Unfortunately, the intrinsic wide bandgap of CeO_2 is inefficient to utilize solar energy, rendering the light-stimulated electron and hole pairs with easy recombination, which leads to unsatisfactory photocatalytic performance.

Recently, numerous studies have shown that defective CeO_2 semiconductors have a high photogenerated carrier migration rate, more adsorption sites, and a narrow bandgap, all of which have a nonnegligible relationship with the oxygen defect on CeO_2.[8a,114] In a recent work, Nie et al. synthesized flower-like $Bi^0/CeO_{2-\delta}$ plasmonic photocatalysts and found that the Schottky barrier between Bi^0 and $CeO_{2-\delta}$ is generated due to the Fermi level imbalance with the introduction of oxygen vacancies, as shown in **Figure 12**a. Thus, the migration of photogenerated carriers is accelerated, which is crucial for the photocatalytic removal of NO (Figure 12b).[115] A similar study by Liang et al. constructed M-ZnO/CeO_2 microsphere plasmonic photocatalysts (M = Ag, Au nanoparticles) and further investigated that the photocatalytic performance was significantly improved with the increase of the oxygen defect concentration, and a synergistic relationship among the heterojunction structure, oxygen defect, and noble metal plasmonic effect was proposed, as shown in Figure 12c.[116] In another work, by doping CeO_2 with Fe, Wang et al. significantly increased the ratio of Ce^{3+}, which means that the concentration of oxygen vacancies significantly increased, which reduced the bandgap of CeO_2 from 2.73 to 1.50 eV. The light absorption range of the sample was extended from the ultraviolet light to the visible light region, as shown in Figure 12d,e, which greatly improved the activity of CeO_2 in catalyzing CO_2 photoreduction to produce CO, methane, and other products under visible light. In the photodegradation of organic pollutants, the oxygen defect of CeO_2 can also play a crucial role in promoting its photocatalytic performance.[114b] Zhang et al. controlled the oxygen vacancy concentration of a composite heterojunction by changing the ratio of air to nitrogen to degrade RhB. They found that when the ratio of air to nitrogen was 2:8, the maximum oxygen vacancy concentration and the highest catalytic activity were obtained.[50] Also, oxygen vacancies promote the formation of the superoxide radical, hydroxyl radical, and photogenerated holes, thus promoting the degradation of pollutants.[117] With regard to the degradation of floxacin antibiotics, it is of great significance to explore the active species and their production pathways to clarify the catalytic mechanism. Therefore, Li et al. studied the active species generated during the degradation of ciprofloxacin over a W-doped CeO_2 catalyst. The results show that oxygen vacancies introduced by W doping can promote the formation of superoxide free radicals and hydroxyl groups, as shown in Figure 12f.[118] In general, although the presence of oxygen defects improves the catalytic performance of CeO_2 in photocatalysis, due to its wide inherent bandgap, it is necessary to combine it with other materials to form a composite catalyst, thus giving full play to the catalytic effect of oxygen defects.

© 2021 Wiley-VCH GmbH

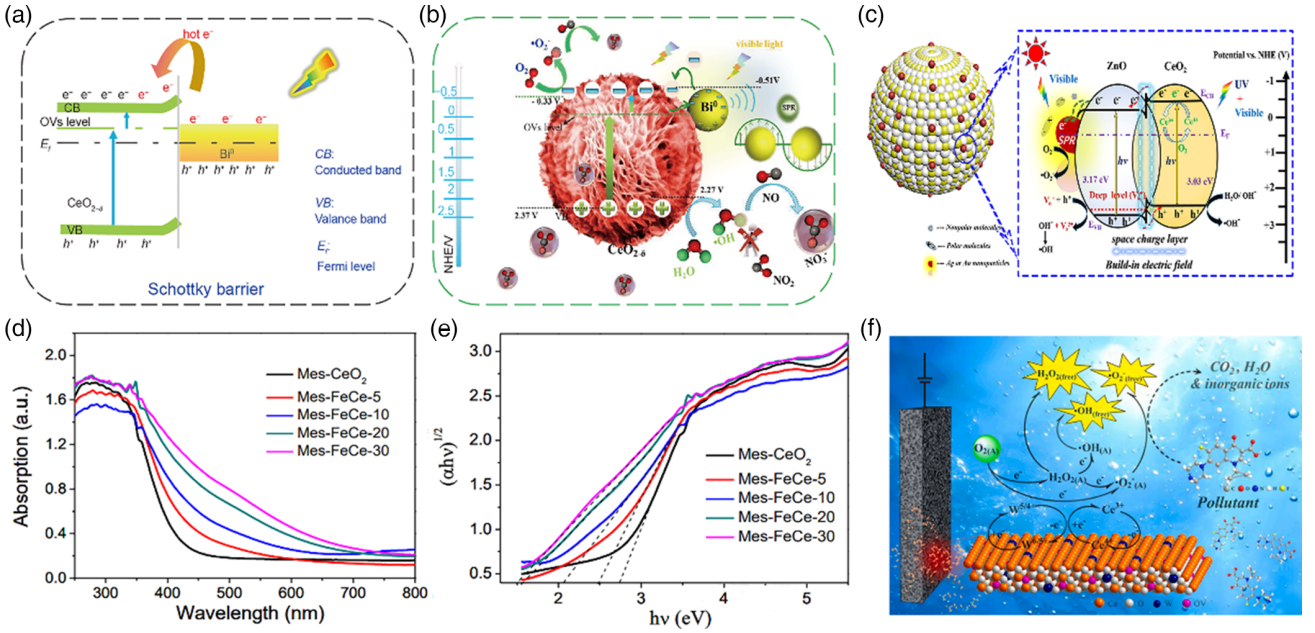


Figure 12. a) The Schottky barrier formed between $Bi^0$and $CeO_{2-\delta}$. b) The proposed mechanism for the photocatalytic NO removal by the $BiO/CeO_{2-\delta}$ photocatalyst. Reproduced with permission.[115] Copyright 2020, Springer Nature. c) Proposed schematic diagram of charge transfer in the M-ZnO/CeO_2 (M = Ag or Au) porous microspheres under UV–vis light irradiation. E_F is the Fermi level; E_{CB} and E_{VB} are the conduction and valence band edges, respectively. Reproduced with permission.[116] Copyright 2020, Elsevier. d) UV–vis diffuse reflectance spectra optical absorption edges and e) Fe-doped CeO_2 nanocatalysts with different ratios of Fe. Reproduced with permission.[114b] Copyright 2014, Elsevier. f) Schematic illustration for ciprofloxacin degradation in the EF-like process. Reproduced with permission.[118] Copyright 2021, Elsevier.

5.6. Biomedical Applications

A large number of studies have shown that oxygen free radicals containing the superoxide free radical, hydrogen peroxide, and hydroxyl radicals have an inseparable relationship with human aging and diseases, so biological antioxidants are considered to be an important research topic. CeO_2 plays an equal role in the catalytic decomposition of these free radicals. Currently, a large number of applications of nanostructured CeO_2 have been developed in biological oxidation resistance due to its abundant and controllable oxygen defects and good biocompatibility. Tan et al. demonstrated that the metastable oxygen vacancies (ms-V_o) on CeO_2 are the crucial factor to promote the reduction of hydrogen peroxide to hydroxyl radical (**Figure 13**a).[117b] The theoretical calculations of free energy (Figure 13b–d) show that the generation of hydroxyl radicals is thermodynamically favorable, in the following order: (100) > (110) > (111). The synergies between structural geometry and chemical states are of great significance to guide the design of catalytic reactions on the surface of CeO_2 using hydrogen peroxide as an oxidizer. Bhalkikar et al. did the same kind of study, but with the difference that they studied in detail the effects of dopants on the total catalytic reaction rate and the apparent activation energy and found that the two trends were not identical (Figure 13e). A new idea was proposed that the dopant Gd^{3+} could slow down the redox cycle between Ce^{3+} and Ce^{4+} by stabilizing the oxygen vacancy defect, thereby reducing turnover rates of the catalytic site.[33] Their method of measuring activity trends related to catalytic and degradation factors is useful for the selection of doped catalysts. Taking advantage of the strong reduction and regeneration capacity of the oxygen vacancy, Shi and his team also chose Gd as the dopant and reported biomimetic superoxide dismutase of CeO_2–Gd nanozymes, and observed the high antioxidant properties and viability of the cells in vitro. The mechanism is shown in Figure 13f. The disproportionation of the enzyme free radical leads to the formation of hydrogen peroxide, and Ce^{3+} regenerates with the formation of electron transfer and oxygen vacancy, finally realizing the inactivation of the superoxide anion.[119] As an antioxidant agent with autoregenerative radical scavenging activity, CeO_2 has been paid extensive attention in the fields of biomedical application. It is well known that the widespread use of biological antioxidants is based on the premise that they can act as chemical spin traps. However, CeO_2 with unique defect structure can provide a number of active sites of spin traps, and it is supposed as a rare material for biological antioxidants. Except for the applications mentioned previously, an increasing number of reviews have been devoted to the ophthalmic,[120] orthopedic,[121] antimicrobial,[122] and anticancer fields.[123] They found that the vacancy-oxygen defect promoted the redox process and catalytic activity and described the corresponding possible mechanism. The antibacterial mechanism of CeO_2 is shown in Figure 13g. CeO_2 nanoparticles kill microorganisms mainly by producing a large amount of reactive oxygen species in large quantities in cells. However, the exact mechanism of microbial destruction and the pathway of oxygen defects and biological toxicities are still not fully understood, and also need to be further explored.

© 2021 Wiley-VCH GmbH

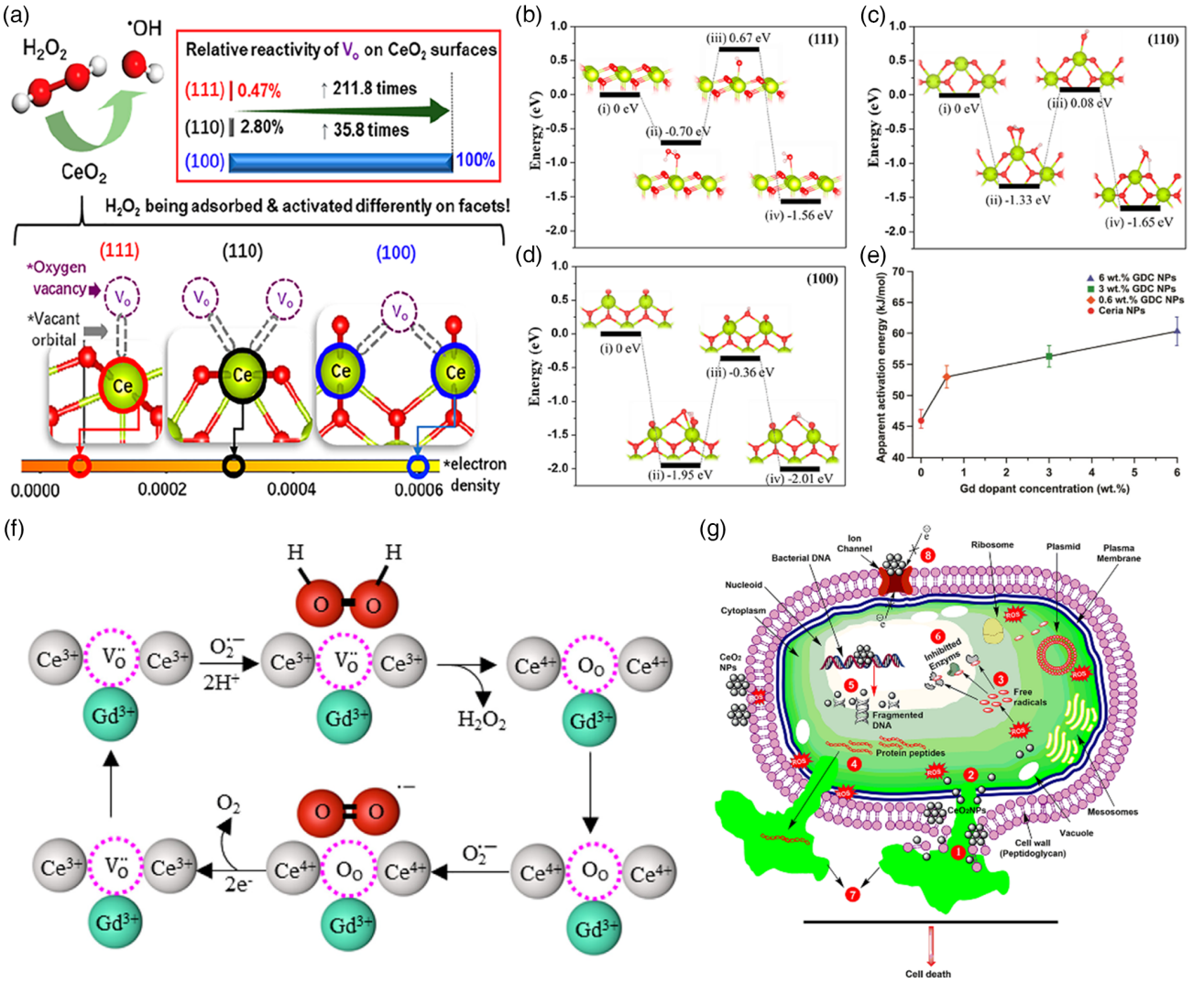


Figure 13. a) Schematic illustration of the activation of adsorbed H_2O_2 on the CeO_2 surface. b–d) The calculated free energy diagrams of H_2O_2 over CeO_2 surfaces: (i) → (ii) the adsorption of H_2O_2 on the CeO_2 surface; (ii) → (iii) O—O bond breakage with the generation of a surface OH group and a OH radical; (iii) → (iv) the formation of H_2O on the CeO_2 surface. a–d) Reproduced with permission.[117b] Copyright 2020, American Chemical Society. e) Plot of apparent activation energy with different Gd dopant concentrations of the GDC NPs. Reproduced with permission.[33] Copyright 2020, Springer. f) Mechanism of superoxide dismutase mimicking activity of CeO_2–Gd nanozyme (right). Reproduced with permission.[119] Copyright 2020, Elsevier. g) Schematic representation of antibacterial activity of CeO_2 nanoparticles. (1) Cell wall disruption; (2) cell membrane disintegration; (3) free radical production; (4) loss of protein peptides; (5) DNA fragmentation; (6) vital enzyme inhibition; (7) loss of cellular fluids; and (8) disruption in electron transport. Reproduced with permission.[127] Copyright 2018, Elsevier.

5.7. Organic Transformation

With the increasing demand for high-value-added chemicals, organic synthesis and transformation, as an effective and feasible method, have been widely studied, but they are mostly limited by the low activity and selectivity of catalysts and cannot be industrialized on a large scale.

Recently, defective-CeO_2-based nanomaterials have attracted extensive attention in aldol condensation, organic oxidation, hydrogenation reduction, and other reactions of organic compounds.[12b,124] Liang et al. controlled the oxygen vacancy concentration on the surface of CeO_2 by controlling the morphology and the atmosphere treatment conditions and then found for the first time that the oxygen vacancy concentration was linearly positively correlated with the aldehyde hydroxyl condensation reaction activity of acetaldehyde. According to the results of in situ infrared study, they suggest that the oxygen vacancies of CeO_2 act as Lewis acid sites, playing a crucial role in activating and stabilizing acetaldehyde molecules.[124a] Recently, plenty of other works have been done on toluene oxidation.[12a,125] For example, Song prepared CeO_2–MnO_x composite catalysts with different cerium sources and applied to toluene oxidation. The results show that the increase of oxygen vacancy increases the concentration of Mn^{3+} and Ce^{3+}, and exhibits excellent oxygen mobility (**Figure 14**a). Consequently,

© 2021 Wiley-VCH GmbH

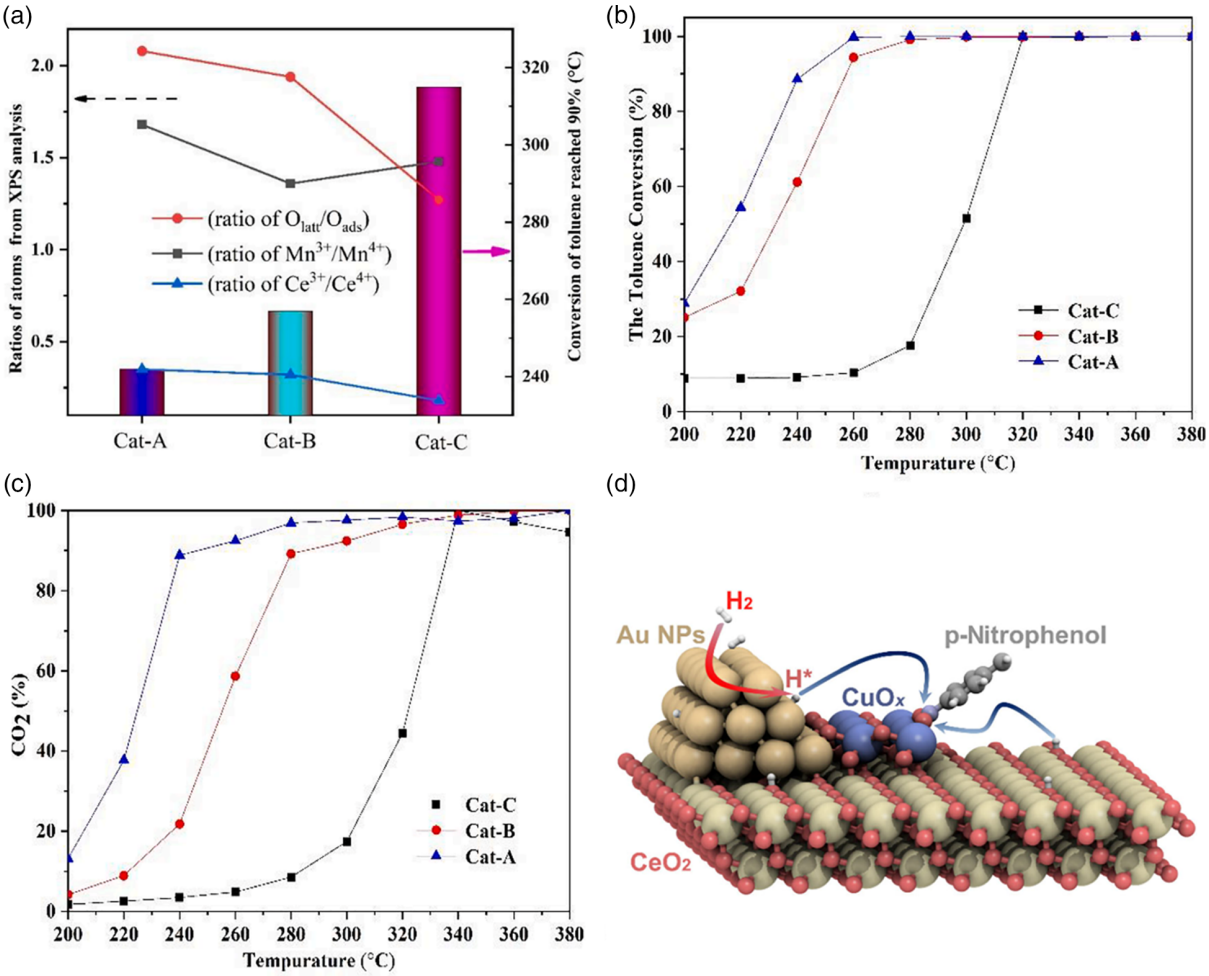


Figure 14. a) The relation between the temperatures of conversion of toluene reaching 90% and the XPS results of catalysts. b) Toluene conversion and c) CO_2 yield as a function of reaction temperature over Cat-A, Cat-B, and Cat-C under the conditions of toluene concentration. a–c) Reproduced with permission.[125a] Copyright 2019, American Chemical Society. d) Schematic illustration for the proposed triphasic synergy catalysis mechanism between the Au/CuO_x/CeO_2 interfaces in Au @CuO_x–CeO_2 core/shell nanospheres. Reproduced with permission.[124c] Copyright 2020, Springer Nature.

the high selection and reaction performance was obtained, as shown in Figure 14b,c.[125a] In addition, hydrogenation reduction as a common reaction has been studied for a few decades.[126] A highly selective Au–CuO_x–CeO_2 core/shell nanosphere catalyst was synthesized by Wu et al. for the catalytic hydrogenation of *p*-nitrophenol. Through the combination of experiments and theoretical simulation, they attributed the high performance of CuO_x–CeO_2-catalyzed hydrogenation of *p*-nitrophenol to the fact that it promotes hydrogen dissociation to form H* species, which contributes to the efficient reduction of *p*-nitrophenol (Figure 14d).[124c] In general, although the oxygen defect of CeO_2 is of signality in catalyzing organic synthesis reactions, its reaction mechanism is very complex and needs to be further studied.

6. Conclusion

In this article, some recent theoretical and experimental results of CeO_2 on defect introductions, characterization, and application in some typical heterogeneous catalysis reactions are reviewed. These results provide valuable references for the further study of the structure–activity relationship between defects and catalytic activity, as well as the mechanism of defects. Generally speaking, three effects of oxygen defects in the system are mainly concluded: 1) offering sites for the adsorption and activation of small molecules (H_2O, CO_2, O_2, N_2); 2) providing sites for metal loading and stabilizing the metal loading; and 3) enhancing the electronic interaction between CeO_2 and metal and increasing the electron density of the metal. Although plenty of studies have been focused on oxygen defects, some key hinders are still to be solved and explored. 1) As described in defect classification, CeO_2 has a variety of defect structures; in addition to oxygen defects, some point defect clusters such as triangle and quadrilateral defects, line defects, and plane defects. However, there are few studies on the application prospects of these defects, most of which focus on the synthesis and structural characterization. Conducting an in-depth study on the application of these defects is of great significance for the perfection of the

© 2021 Wiley-VCH GmbH

CeO_2 defect chemistry system and the large-scale application of CeO_2-based catalysts. 2) In recent years, we grasped a detailed basic understanding of the specific optimization of CeO_2 catalysts. However, more accurate and controllable methods for synthesizing of high-concentration oxygen vacancies and the optimal concentration of specific applications are still the key factors limiting further development. To our best knowledge, previous studies used different methods to obtain a relatively high concentration of defects. However, there are few studies on how the specific defect content affects the catalytic performance. Therefore, the development of more uniform, efficient, and low-cost synthesis methods remains a significant challenge to optimize the defect structure of CeO_2-based materials. We are looking forward to advanced reports that can realize the controllable synthesis of defects and control the defect concentration of CeO_2 to get a better catalytic effect. 3) Characterizations and the dynamics evolution process of oxygen defects in previous studies are still deficient. To our best knowledge, most of the characterizations are qualitative or semiquantitative. Although there are some in situ characterizations of defect content that can be characterized by calculating the diffraction of the Ce^{3+} peak area, intuitive and accurate quantitative analyses of the concentration of oxygen defects are still lacking. In addition, to discuss the dynamic evolution process of the defect structure, new supervised technologies urgently need to be constructed. We expect an increasing number of researchers are engaged in exploring this project hoping to gain a thorough knowledge system of defective CeO_2. 4) Many researchers have proposed corresponding mechanisms for their respective catalytic reactions, but many current viewpoints are one-sided, and the understanding of the knowledge system of oxygen defects is not very comprehensive. Therefore, the structure–activity relationship and potential mechanism between oxygen defects and catalytic activity in heterogeneous catalysis need to be further explored. 5) We reviewed the applied areas of defective-CeO_2-based catalysts in recent years, but the application should continue to be expanded according to the unique properties of CeO_2 with oxygen defects. We can explore its application in other types of new fields such as oxygen permeation membranes, sensors, and organic electrocatalytic synthesis, which are of great value in promoting more directions of heterogeneous catalysis.

These are also the improvement directions we put forward based on the future exploration and development of defective CeO_2. In this review, it is our primary purpose to provide readers with the essential background of the introduction methods and practical applications of defective CeO_2 catalysts and the latest research progress. It is expected to provide references for the better design of defective heterogeneous catalysts to promote the activity, selectivity, and stability of heterogeneous catalytic reactions.

Acknowledgements

C. Y. and Y. L. contributed equally to this work. This work was supported by the National Key R&D Program of China (2020YFA0710000), the National Natural Science Foundation of China (grant Nos. 21902047, 21825201, U19A2017), the Provincial Natural Science Foundation of Hunan (2016TP1009 and 2020JJ5045), and the Changsha Municipal Natural Science Foundation (kq2007007).

Conflict of Interest

The authors declare no conflict of interest.

Keywords

CeO_2, defect engineering, heterogeneous catalytics, structure–activity relationship

Received: May 4, 2021
Revised: July 5, 2021
Published online: September 5, 2021

[1] a) W. Xu, K. B. Thapa, Q. Ju, Z. Fang, W. Huang, *Coord. Chem. Rev.* **2018**, *373*, 199; b) T. Mathew, S. Saju, S. N. Raveendran, *Engineering Solutions for CO2 Conversion*, John Wiley & Sons, Inc., Hoboken, NJ **2021**, pp. 335-360.
[2] a) M. Boudart, G. Djéga-Mariadassou, *Kinetics of Heterogeneous Catalytic Reactions*, Princeton University Press, Princeton **2014**; b) R. M. Kulkarni, P. J. Britto, A. Narula, S. Saqline, D. Anand, C. Bhagyalakshmi, R. N. Herle, *Biofuel Res. J.* **2020**, *7*, 1100.
[3] a) F. Kroger, *Annu. Rev. Mater. Sci.* **1977**, *7*, 449. b) X. Yan, Y. Jia, X. Yao, *Small Struct.* **2021**, *2*, 2000067.
[4] S. G. Motti, D. Meggiolaro, S. Martani, R. Sorrentino, A. J. Barker, F. De Angelis, A. Petrozza, *Adv. Mater.* **2019**, *31*, 1901183.
[5] a) W. Li, D. Wang, Y. Zhang, L. Tao, T. Wang, Y. Zou, Y. Wang, R. Chen, S. Wang, *Adv. Mater.* **2020**, *32*, 1907879; b) Y. Zhang, L. Tao, C. Xie, D. Wang, Y. Zou, R. Chen, Y. Wang, C. Jia, S. Wang, *Adv. Mater.* **2020**, *32*, 1905923; c) D. Yan, Y. Li, J. Huo, R. Chen, L. Dai, S. Wang, *Adv. Mater.* **2017**, *29*, 1606459; d) C. Xie, D. Yan, H. Li, S. Du, W. Chen, Y. Wang, Y. Zou, R. Chen, S. Wang, *ACS Catal.* **2020**, *10*, 11082.
[6] W. Yang, X. Wang, S. Song, H. Zhang, *Chem* **2019**, *5*, 1743.
[7] a) Y. Xie, J. Wu, G. Jing, H. Zhang, S. Zeng, X. Tian, X. Zou, J. Wen, H. Su, C.-J. Zhong, P. Cui, *Appl. Catal. B, Environ* **2018**, *239*, 665; b) X. Ye, H. Wang, Y. Lin, X. Liu, L. Cao, J. Gu, J. Lu, *Nano Res.* **2019**, *12*, 1401.
[8] a) C. Yang, Q. Li, Y. Xia, K. Lv, M. Li, *Appl. Surf. Sci.* **2019**, *464*, 388; b) Y. Pu, Y. Luo, X. Wei, J. Sun, L. Li, W. Zou, L. Dong, *Appl. Catal. B, Environ* **2019**, *254*, 580; c) Y. Wang, Z. Chen, P. Han, Y. Du, Z. Gu, X. Xu, G. Zheng, *ACS Catal.* **2018**, *8*, 7113.
[9] a) J. Yu, J. Wang, X. Long, L. Chen, Q. Cao, J. Wang, C. Qiu, J. Lim, S. Yang, *Adv. Energy. Mater.* **2021**, *11*, 2002731; b) L. Yang, R. Liu, L. Jiao, *Adv. Funct. Mater.* **2020**, *30*, 1909618.
[10] a) R. Ma, S. Zhang, T. Wen, P. Gu, L. Li, G. Zhao, F. Niu, Q. Huang, Z. Tang, X. Wang, *Catal. Today* **2019**, *335*, 20; b) A. Wang, Z. Zheng, H. Wang, Y. Chen, C. Luo, D. Liang, B. Hu, R. Qiu, K. Yan, *Appl. Catal. B, Environ* **2020**, *277*, 119171.
[11] X. Zhang, X. Chen, *Int. J. Polym. Sci.* **2019**, *2019*, 2494586.
[12] a) B. Dou, D. Yang, T. Kang, Y. Xu, Q. Hao, F. Bin, X. Xu, *Carbon Resour. Convers.* **2021**, *4*, 55; b) Y. Long, J. Li, L. Wu, Q. Wang, Y. Liu, X. Wang, S. Song, H. Zhang, *Nano Res.* **2019**, *12*, 869.
[13] R. A. Amoresi, R. C. Oliveira, N. L. Marana, P. B. De Almeida, P. S. Prata, M. A. Zaghete, E. Longo, J. R. Sambrano, A. Z. Simoes, *ACS Appl. Nano Mater.* **2019**, *2*, 6513.

© 2021 Wiley-VCH GmbH

[14] C. Sun, H. Li, L. Chen, *Energy Environ. Sci.* **2012**, *5*, 8475.
[15] M. Melchionna, P. Fornasiero, *Mater. Today* **2014**, *17*, 349.
[16] M. Mogensen, N. M. Sammes, G. A. Tompsett, *Solid State Ionics* **2000**, *129*, 63.
[17] a) C. Sun, H. Li, L. Chen, *Energy Environ. Sci.* **2012**, *5*, 8475; b) J. Liu, M. Dai, T. Wang, P. Sun, X. Liang, G. Lu, K. Shimanoe, N. Yamazoe, *ACS Appl. Mater. Interfaces* **2016**, *8*, 6669.
[18] S. R. Bishop, T. S. Stefanik, H. L. Tuller, *Phys. Chem. Chem. Phys.* **2011**, *13*, 10165.
[19] a) H. Hojo, E. Tochigi, T. Mizoguchi, H. Ohta, N. Shibata, B. Feng, Y. Ikuhara, *Appl. Phys. Lett.* **2011**, *98*, 153104; b) K. Yasunaga, K. Yasuda, S. Matsumura, T. Sonoda, *Nucl. Instrum. Meth. B* **2008**, *266*, 2877; c) K. Yasunaga, K. Yasuda, S. Matsumura, T. Sonoda, *Nucl. Instrum. Meth. B* **2006**, *250*, 114; d) Y. Kun, Y. Zhang, *J. Rare Earth* **2020**, *38*, 326.
[20] a) B. Feng, H. Hojo, T. Mizoguchi, H. Ohta, S. Findlay, Y. Sato, N. Shibata, T. Yamamoto, Y. Ikuhara, *Appl. Phys. Lett.* **2012**, *100*, 073109; b) H. Hojo, T. Mizoguchi, H. Ohta, S. D. Findlay, N. Shibata, T. Yamamoto, Y. Ikuhara, *Nano Lett.* **2010**, *10*, 4668.
[21] a) F. Esch, S. Fabris, L. Zhou, T. Montini, C. Africh, P. Fornasiero, G. Comelli, R. Rosei, *Science* **2005**, *309*, 752; b) S. Agarwal, X. Zhu, E. Hensen, B. Mojet, L. Lefferts, *J. Phys. Chem. C* **2015**, *119*, 12423.
[22] a) Z. Wu, M. Li, J. Howe, H. M. Meyer III, S. H. Overbury, *Langmuir* **2010**, *26*, 16595; b) T. Zacherle, A. Schriever, R. De Souza, M. Martin, *Phys. Rev. B* **2013**, *87*, 134104.
[23] a) R. Si, Y. W. Zhang, S. J. Li, B. X. Lin, C. H. Yan, *J. Phys. Chem. B* **2004**, *108*, 12481; b) A. B. Kehoe, D. O. Scanlon, G. W. Watson, *Chem. Mater.* **2011**, *23*, 4464.
[24] K. i. Fukui, Y. Namai, Y. Iwasawa, *Appl. Surf. Sci.* **2002**, *188*, 252.
[25] C. Jiang, H. Wang, Y. Wang, C. Xue, Z. Yang, C. Yu, H. Ji, *J. Hazard. Mater.* **2020**, *390*, 122182.
[26] a) M. Kumar, J. H. Yun, V. Bhatt, B. Singh, J. Kim, J. S. Kim, B. S. Kim, C. Y. Lee, *Electrochim. Acta* **2018**, *284*, 709; b) M. Dosa, M. Piumetti, S. Bensaid, T. Andana, C. Novara, F. Giorgis, D. Fino, N. Russo, *Catal. Lett.* **2018**, *148*, 298; c) X. Ma, P. Lu, P. Wu, *Ceram. Int.* **2018**, *44*, 15989.
[27] C. A. Chagas, E. F. de Souza, R. L. Manfro, S. M. Landi, M. M. Souza, M. Schmal, *Appl. Catal. B, Environ* **2016**, *182*, 257.
[28] W. Wang, Q. Zhu, Q. Dai, X. Wang, *Chem. Eng. J.* **2017**, *307*, 1037.
[29] I. Kosacki, V. Petrovsky, H. U. Anderson, P. Colomban, *J. Am. Ceram. Soc.* **2002**, *85*, 2646.
[30] S. Tiwari, N. Khatun, N. Patra, A. Yadav, D. Bhattacharya, S. Jha, C. Tseng, S. Liu, S. Biring, S. Sen, *Ceram. Int.* **2019**, *45*, 3823.
[31] S. Soni, M. Dave, B. Dalela, P. Alvi, S. Kumar, S. Sharma, D. Phase, M. Gupta, S. Dalela, *Appl. Phys. A* **2020**, *126*, 1.
[32] S. Zhao, D. Kang, Y. Liu, Y. Wen, X. Xie, H. Yi, X. Tang, *ACS Catal.* **2020**, *10*, 11739.
[33] A. Bhalkikar, T. S. Wu, T. J. Fisher, A. Sarella, D. Zhang, Y. Gao, Y. L. Soo, C. L. Cheung, *Nano Res.* **2020**, *13*, 2384.
[34] J. Huang, Y. Yu, J. Zhu, R. Yu, *Sci. China Technol. Sci.* **2018**, *61*, 135.
[35] J. L. Lu, H. J. Gao, S. Shaikhutdinov, H. J. Freund, *Surf. Sci.* **2006**, *600*, 5004.
[36] Y. Chang, Y. Guo, M. Li, K. Wang, L. Lv, D. Liu, *J. Nucl. Mater.* **2019**, *518*, 41.
[37] a) R. Schmitt, A. Nenning, O. Kraynis, R. Korobko, A. I. Frenkel, I. Lubomirsky, S. M. Haile, J. L. Rupp, *Chem. Soc. Rev.* **2020**, *49*, 554; b) M. Ziemba, C. Schilling, M. V. Ganduglia-Pirovano, C. Hess, *Acc. Chem. Res.* **2021**, 6593; c) C. Schilling, C. Hess, *J. Phys. Chem. C* **2018**, *122*, 2909; d) A.-K. Elger, J. Baranyai, K. Hofmann, C. Hess, *ACS Sens.* **2019**, *4*, 1497.
[38] J. A. Rodriguez, P. Liu, J. Hrbek, J. Evans, M. Pérez, *Angew. Chem., Int. Ed.* **2010**, *46*, 1329.
[39] Y. Li, J. Lin, B. Xie, G. Liu, *J Wuhan Univ. Technol.* **2020**, *35*, 335.
[40] a) J. Hernández-Arteaga, H. Moreno-García, A. Rodríguez, *Thin Solid Films* **2021**, 138602; b) X. Han, N. Amrane, Z. Zhang, M. Benkraouda, *Chem. Phys.* **2020**, *534*, 110741.
[41] a) A. B. Kharissova, M. H. Rivera, O. V. Kharissova, *MRS Adv.* **2018**, *3*, 1855; b) S. Soni, S. Kumar, B. Dalela, S. Kumar, P. Alvi, S. Dalela, *J. Alloys Compd.* **2018**, *752*, 520; c) P. Wang, J. Wang, J. Shi, X. Du, X. Hao, B. Tang, A. Abudula, G. Guan, *Mol. Catal.* **2020**, *492*, 111027.
[42] H. Khakhal, S. Kumar, S. Dolia, B. Dalela, V. Vats, S. Z. Hashmi, P. Alvi, S. Kumar, S. Dalela, *J. Alloys Compd.* **2020**, *844*, 156079.
[43] a) X. Yu, X. Wu, Z. Chen, Z. Huang, G. Jing, *Mol. Catal.* **2019**, *476*, 110512; b) B. Qiu, C. Wang, N. Zhang, L. Cai, Y. Xiong, Y. Chai, *ACS Catal.* **2019**, *9*, 6484; c) M. M. Khan, W. Khan, M. Ahamed, A. N. Alhazaa, *Sci. Rep.* **2017**, *7*, 1.
[44] S. B. Varandili, J. Huang, E. Oveisi, G. L. De Gregorio, M. Mensi, M. Strach, J. Vavra, C. Gadiyar, A. Bhowmik, R. Buonsanti, *ACS Catal.* **2019**, *9*, 5035.
[45] H. Dong, L. Zhang, L. Li, W. Deng, C. Hu, Z. J. Zhao, J. Gong, *Small* **2019**, *15*, 1900289.
[46] L. Zeng, L. Cui, C. Wang, W. Guo, C. Gong, *Front. Mater. Sci.* **2019**, *13*, 288.
[47] a) M. C. Spadaro, S. D'Addato, G. Gasperi, F. Benedetti, P. Luches, V. Grillo, G. Bertoni, S. Valeri, *Beilstein J. Nanotechnol.* **2015**, *6*, 60; b) X. Liu, K. Zhou, L. Wang, B. Wang, Y. Li, *J. Am. Chem. Soc.* **2009**, *131*, 3140; c) C. M. Kalamaras, S. Americanou, A. M. Efstathiou, *J. Catal.* **2011**, *279*, 287.
[48] G. B. Della Mea, L. P. Matte, A. S. Thill, F. O. Lobato, E. V. Benvenutti, L. T. Arenas, A. Jürgensen, R. Hergenroder, F. Poletto, F. Bernardi, *Appl. Surf. Sci.* **2017**, *422*, 1102.
[49] C. Chen, Y. Zhan, J. Zhou, D. Li, Y. Zhang, X. Lin, L. Jiang, Q. Zheng, *ChemPhysChem* **2018**, *19*, 1448.
[50] Q. Zhang, X. Zhao, L. Duan, H. Shen, R. Liu, *J. Photoch. Photobio. A* **2020**, *392*, 112156.
[51] a) A. Murali, Y. Lan, P. Sarswat, M. Free, *Mater. Today Chem.* **2019**, *12*, 222; b) D. Oró, T. Yudina, G. Fernández-Varo, E. Casals, V. Reichenbach, G. Casals, B. G. de la Presa, S. Sandalinas, S. Carvajal, V. Puntes, *J. Hepatol.* **2016**, *64*, 691; c) J. Carrillo-Rodríguez, S. García-Mayagoitia, R. Pérez-Hernández, M. Ochoa-Lara, F. Espinosa-Magaña, F. Fernández-Luqueño, I. Alonso-Lemus, F. Rodriguez-Varela, *ECS Trans.* **2017**, *77*, 1359; d) A. Nozaki, C. Ueda, R. Fujiwara, A. Yamashita, H. Yamamoto, M. Morishita, *Mater. Trans.* **2019**, *60*, 845.
[52] M. Konsolakis, M. Lykaki, *Catalysts* **2020**, *10*, 160.
[53] W. Gao, J. Li, X. Zhou, Z. Zhang, Y. Ma, Y. Qu, *J. Mater. Chem. C* **2014**, *2*, 8729.
[54] W. Gao, Z. Zhang, J. Li, Y. Ma, Y. Qu, *Nanoscale* **2015**, *7*, 11686.
[55] a) S. Totong, P. Daorattanachai, N. Laosiripojana, R. Idem, *Fuel Process. Technol.* **2020**, *198*, 106248; b) T. Furusawa, K. Sugiyama, H. Kuribara, M. Sato, N. Suzuki, T. Sato, N. Itoh, *J. Chem. Eng. Jpn.* **2021**, *54*, 77.
[56] Y. Wang, Z. Liu, R. Wang, *ChemCatChem* **2020**, *12*, 4304.
[57] S. Deshpande, S. Patil, S. V. Kuchibhatla, S. Seal, *Appl. Phys. Lett.* **2005**, *87*, 133113.
[58] a) A. Migani, G. N. Vayssilov, S. T. Bromley, F. Illas, K. M. Neyman, *J. Mater. Chem.* **2010**, *20*, 10535; b) M. A. Sk, S. M. Kozlov, K. H. Lim, A. Migani, K. M. Neyman, *J. Mater. Chem. A* **2014**, *2*, 18329; c) A. Bruix, K. M. Neyman, *Catal. Lett.* **2016**, *146*, 2053.
[59] a) S. Carrettin, P. Concepción, A. Corma, J. M. Lopez Nieto, V. F. Puntes, *Angew. Chem., Int. Ed.* **2004**, *43*, 2538; b) J. Guzman, S. Carrettin, A. Corma, *J. Am. Chem. Soc.* **2005**, *127*, 3286; c) A. Migani, G. N. Vayssilov, S. T. Bromley, F. Illas, K. M. Neyman, *Chem. Commun.* **2010**, *46*, 5936.

 © 2021 Wiley-VCH GmbH

[60] a) H. X. Mai, L. D. Sun, Y. W. Zhang, R. Si, W. Feng, H. P. Zhang, H. C. Liu, C. H. Yan, *J. Mater. Chem. B* **2005**, *109*, 24380; b) Z. Feng, Q. Ren, R. Peng, S. Mo, M. Zhang, M. Fu, L. Chen, D. Ye, *Catal. Today* **2019**, *332*, 177.
[61] a) Y. Wang, C. Woll, *Chem. Soc. Rev.* **2017**, *46*, 1875; b) T. Montini, M. Melchionna, M. Monai, P. Fornasiero, *Chem. Rev.* **2016**, *116*, 5987; c) A. Trovarelli, J. Llorca, *ACS Catal.* **2017**, *7*, 4716.
[62] W. Lei, T. Zhang, L. Gu, P. Liu, J. A. Rodriguez, G. Liu, M. Liu, *ACS Catal.* **2015**, *5*, 4385.
[63] R. Si, M. Flytzani-Stephanopoulos, *Angew. Chem., Int. Ed.* **2008**, *120*, 2926.
[64] Y. Sun, Q. Liu, S. Gao, H. Cheng, F. Lei, Z. Sun, Y. Jiang, H. Su, S. Wei, Y. Xie, *Nat. Commun.* **2013**, *4*, 1.
[65] E. Paparazzo, *Surf. Sci.* **1990**, *234*, L253.
[66] M. R. Rao, T. Shripathi, *J. Electron Spectrosc. Relat. Phenom.* **1997**, *87*, 121.
[67] L. Qiu, F. Liu, L. Zhao, Y. Ma, J. Yao, *Appl. Surf. Sci.* **2006**, *252*, 4931.
[68] J. Holgado, G. Munuera, J. Espinós, A. González-Elipe, *Appl. Surf. Sci.* **2000**, *158*, 164.
[69] G. Wang, D. Kong, Y. Pan, H. Pan, J. Zhu, *Appl. Surf. Sci.* **2012**, *258*, 2057.
[70] a) Y. Zhang, P. D. Edmondson, T. Varga, S. Moll, F. Namavar, C. Lan, W. J. Weber, *Phys. Chem. Chem. Phys.* **2011**, *13*, 11946; b) P. Ramasamy, S. Guha, E. S. Shibu, T. S. Sreeprasad, S. Bag, A. Banerjee, T. Pradeep, *J. Mater. Chem.* **2009**, *19*, 8456; c) B. Tatar, E. Sam, K. Kutlu, M. Ürgen, *J. Mater. Sci.* **2008**, *43*, 5102; d) M. M. Khan, S. A. Ansari, D. Pradhan, M. O. Ansari, J. Lee, M. H. Cho, *J. Mater. Chem. A* **2014**, *2*, 637; e) Y. Ding, Y. Choi, Y. Chen, K. C. Pradel, M. Liu, Z. L. Wang, *Mater. Today* **2020**, *38*, 24; f) R. I. Palomares, C. L. Tracy, F. Zhang, C. Park, D. Popov, C. Trautmann, R. C. Ewing, M. Lang, *J. Appl. Crystallogr.* **2015**, *48*, 711.
[71] M. M. Khan, S. A. Ansari, D. Pradhan, D. H. Han, J. Lee, M. H. Cho, *Ind. Eng. Chem. Res.* **2014**, *53*, 9754.
[72] W. Ren, D. Tang, M. Huang, J. Sun, K. Lv, *J. Hazard. Mater.* **2018**, *350*, 88.
[73] S. Hinokuma, N. Yamashita, Y. Katsuhara, H. Kogami, M. Machida, *Catal. Sci. Technol.* **2015**, *5*, 3945.
[74] Y. Xie, J. Wu, G. Jing, H. Zhang, S. Zeng, X. Tian, X. Zou, J. Wen, H. Su, C.-J. Zhong, *Appl. Catal. B, Environ.* **2018**, *239*, 665.
[75] a) L. Liu, A. Corma, *Chem. Rev.* **2018**, *118*, 4981; b) H. Yoshida, R. Kakei, Y. Kuzuhara, S. Misumi, M. Machida, *Catal. Today* **2019**, *332*, 245.
[76] A. Chen, X. Yu, Y. Zhou, S. Miao, Y. Li, S. Kuld, J. Sehested, J. Liu, T. Aoki, S. Hong, *Nat. Catal.* **2019**, *2*, 334.
[77] J. Ke, W. Zhu, Y. Jiang, R. Si, Y.-J. Wang, S.-C. Li, C. Jin, H. Liu, W.-G. Song, C.-H. Yan, *ACS Catal.* **2015**, *5*, 5164.
[78] a) P. Salarizadeh, M. B. Askari, M. Mohammadi, K. Hooshyari, *J. Phys. Chem. Solids* **2020**, *142*, 109442; b) L. Tao, Y. Shi, Y. C. Huang, R. Chen, Y. Zhang, J. Huo, Y. Zou, G. Yu, J. Luo, C. L. Dong, *Nano Energy* **2018**, *53*, 604.
[79] W. Li, Q. Wang, L. Wang, X. Z. Fu, J. L. Luo, *J. Rare Earths* **2020**, *36*, 674.
[80] Z. Jiang, M. Jing, X. Feng, J. Xiong, C. He, M. Douthwaite, L. Zheng, W. Song, J. Liu, Z. Qu, *Appl. Catal. B, Environ.* **2020**, *278*, 119304.
[81] C. Liu, L. Zhang, L. Sun, W. Wang, Z. Chen, *Int. J. Hydrog. Energy* **2020**, *45*, 8558.
[82] a) X. Zong, J. Zhang, J. Zhang, W. Luo, A. Züttel, Y. Xiong, *Electrochem. Commun.* **2020**, *114*, 106716; b) L. R. Winter, R. Chen, X. Chen, K. Chang, Z. Liu, S. D. Senanayake, A. M. Ebrahim, J. G. Chen, *Appl. Catal. B, Environ.* **2019**, *245*, 360.
[83] Q. Zhang, J. Du, A. He, Z. Liu, C. Tao, *J. Solid State Chem.* **2019**, *279*, 120946.
[84] M. Luo, Z. Wang, Y. C. Li, J. Li, F. Li, Y. Lum, D.-H. Nam, B. Chen, J. Wicks, A. Xu, *Nat. Commun.* **2019**, *10*, 1.
[85] D. Gao, Y. Zhang, Z. Zhou, F. Cai, X. Zhao, W. Huang, Y. Li, J. Zhu, P. Liu, F. Yang, *J. Am. Chem. Soc.* **2017**, *139*, 5652.
[86] E. Verlato, S. Barison, Y. Einaga, S. Fasolin, M. Musiani, L. Nasi, K. Natsui, F. Paolucci, G. Valenti, *J. Mater. Chem. A* **2019**, *7*, 17896.
[87] Y. Yang, S. Wang, Y. Jiang, X. Wu, C. Xia, R. Peng, Y. Lu, *J. Phys. Chem. C* **2019**, *123*, 17092.
[88] a) M. Liang, T. Borjigin, Y. Zhang, B. Liu, H. Liu, H. Guo, *Appl. Catal. B, Environ.* **2019**, *243*, 566; b) M. Wang, M. Shen, X. Jin, J. Tian, M. Li, Y. Zhou, L. Zhang, Y. Li, J. Shi, *ACS Catal.* **2019**, *9*, 4573; c) Y. Wang, X. Bai, F. Wang, S. Kang, C. Yin, X. Li, *J. Hazard. Mater.* **2019**, *372*, 69.
[89] a) H. Shen, T. Peppel, J. Strunk, Z. Sun, *Solar RRL* **2020**, *4*, 1900546; b) H. Shen, C. Choi, J. Masa, X. Li, J. Qiu, Y. Jung, Z. Sun, *Chem* **2021**, *7*, 1708.
[90] X. Feng, H. Chen, F. Jiang, X. Wang, *Catal. Sci. Technol.* **2019**, *9*, 2849.
[91] a) X. Zhu, S. Mou, Q. Peng, Q. Liu, Y. Luo, G. Chen, S. Gao, X. Sun, *J. Mater. Chem. A* **2020**, *8*, 1545; b) X. Guo, H. Du, F. Qu, J. Li, *J. Mater. Chem. A* **2019**, *7*, 3531.
[92] Y. Ding, L. Huang, J. Zhang, A. Guan, Q. Wang, L. Qian, L. Zhang, G. Zheng, *J. Mater. Chem. A* **2020**, *8*, 7229.
[93] B. Xu, L. Xia, F. Zhou, R. Zhao, H. Chen, T. Wang, Q. Zhou, Q. Liu, G. Cui, X. Xiong, *ACS Sustain. Chem. Eng.* **2019**, *7*, 2889.
[94] G. Liu, Z. Cui, M. Han, S. Zhang, C. Zhao, C. Chen, G. Wang, H. Zhang, *Chem. Eur. J.* **2019**, *25*, 5904.
[95] L. Chen, H. Jang, M. G. Kim, Q. Qin, X. Liu, J. Cho, *Inorg. Chem. Front.* **2020**, *7*, 470.
[96] H. Sun, C. Tian, G. Fan, J. Qi, Z. Liu, Z. Yan, F. Cheng, J. Chen, C. P. Li, M. Du, *Adv. Funct. Mater.* **2020**, *30*, 1910596.
[97] J. J. Zhang, W. W. Bao, M. Y. Li, C. M. Yang, N. N. Zhang, *Chem. Commun.* **2020**, *56*, 14713.
[98] J. Liu, Y. Gao, Y. Wei, X. Chen, S. Hao, X. Ding, L. Pan, *Chem. Commun.* **2020**, *56*, 4228.
[99] a) J. Xia, H. Zhao, B. Huang, L. Xu, M. Luo, J. Wang, F. Luo, Y. Du, C. H. Yan, *Adv. Funct. Mater.* **2020**, *30*, 1908367. b) J. J. Zhang, C. M. Yang, C. Q. Jin, W. W. Bao, R. H. Nan, L. Hu, G. Liu, N. N. Zhang, *Chem. Commun.* **2021**, *57*, 3563.
[100] a) J. X. Feng, S. H. Ye, H. Xu, Y. X. Tong, G. R. Li, *Adv. Mater.* **2016**, *28*, 4698; b) H. Lim, J. Y. Kim, E. Evans, A. Rai, J.-H. Kim, B. R. Wygant, C. B. Mullins, *ACS Appl. Mater. Interfaces* **2017**, *9*, 30654.
[101] a) M. Li, X. Pan, M. Jiang, Y. Zhang, Y. Tang, G. Fu, *Chem. Eng. J.* **2020**, *395*, 125160; b) C. Yang, C. Wang, L. Zhou, W. Duan, Y. Song, F. Zhang, Y. Zhen, J. Zhang, W. Bao, Y. Lu, *Chem. Eng. J.* **2021**, *422*, 130125.
[102] H. Feng, Z. Xu, L. Ren, C. Liu, J. Zhuang, Z. Hu, X. Xu, J. Chen, J. Wang, W. Hao, *ACS Catal.* **2018**, *8*, 4288.
[103] Y. Zhao, T. Ling, S. Chen, B. Jin, A. Vasileff, Y. Jiao, L. Song, J. Luo, S. Z. Qiao, *Angew. Chem., Int. Ed.* **2019**, *58*, 12252.
[104] a) N. Yao, R. Meng, F. Wu, Z. Fan, G. Cheng, W. Luo, *Appl. Catal. B: Environ.* **2020**, *277*, 119282; b) C. Wang, X. Lv, P. Zhou, X. Liang, Z. Wang, Y. Liu, P. Wang, Z. Zheng, Y. Dai, Y. Li, *ACS Appl. Mater. Interfaces* **2020**, *12*, 29153.
[105] M. C. Sung, G. H. Lee, D. W. Kim, *J. Alloys Compd.* **2019**, *800*, 450.
[106] C. Zhang, W. Zhang, N. E. Drewett, X. Wang, S. J. Yoo, H. Wang, T. Deng, J. G. Kim, H. Chen, K. Huang, *ChemSusChem* **2019**, *12*, 1000.
[107] H. Sun, C. Tian, Y. Li, J. Wu, Q. Wang, Z. Yan, C. P. Li, F. Cheng, M. Du, *Adv. Sustain. Syst.* **2020**, *4*, 2000122.
[108] A. Krishnan, M. A. Sha, R. Basheer, A. Riyas, S. Shibli, *Mater. Sci. Semicond. Process.* **2020**, *116*, 105138.

© 2021 Wiley-VCH GmbH

[109] F. Shen, K. Lu, *ACS Appl. Mater. Interfaces* **2017**, *9*, 6022.
[110] Y. Xing, M. Akbar, M. Yousaf, M. Y. Shah, C. Xia, J. Gao, X. Wang, *Int. J. Hydrog. Energy* **2021**, *46*, 9855.
[111] a) M. Akbar, Z. Tu, B. Jin, N. Mushtaq, Z. He, W. Dong, B. Wang, X. Wang, C. Xia, *Int. J. Hydrog. Energy* **2021**, *46*, 9938; b) W. Zhang, H. Wang, K. Guan, Z. Wei, X. Zhang, J. Meng, X. Liu, J. Meng, *ACS Appl. Mater. Interfaces* **2019**, *11*, 26830; c) Z. Qiao, C. Xia, Y. Cai, M. Afzal, H. Wang, J. Qiao, B. Zhu, *J. Power Sources* **2018**, *392*, 33; d) B. C. Yang, D. Go, S. Oh, J. W. Shin, H. J. Kim, J. An, *Appl. Surf. Sci.* **2019**, *473*, 102.
[112] L. Li, B. Zhu, J. Zhang, C. Yan, Y. Wu, *Int. J. Hydrog. Energy* **2018**, *43*, 12909.
[113] a) B. Zhao, Q. Shao, L. Hao, L. Zhang, Z. Liu, B. Zhang, S. Ge, Z. Guo, *J. Colloid Interface Sci.* **2018**, *511*, 39; b) T. Jia, J. Wu, Y. Xiao, Q. Liu, Q. Wu, Y. Qi, X. Qi, *J. Colloid Interface Sci.* **2021**, *587*, 402.
[114] a) M. Li, P. Wang, Z. Ji, Z. Zhou, Y. Xia, Y. Li, S. Zhan, *Appl. Catal. B, Environ.* **2021**, *289*, 120020; b) Y. Wang, F. Wang, Y. Chen, D. Zhang, B. Li, S. Kang, X. Li, L. Cui, *Appl. Catal. B, Environ.* **2014**, *147*, 602.
[115] J. Nie, J. Gao, Q. Shen, W. Zhang, F. Rao, M. Hojamberdiev, G. Zhu, *Sci. China Mater.* **2020**, *63*, 2272.
[116] X. Liang, P. Wang, Y. Gao, H. Huang, F. Tong, Q. Zhang, Z. Wang, Y. Liu, Z. Zheng, Y. Dai, *Appl. Catal. B, Environ.* **2020**, *260*, 118151.
[117] a) C. Yang, J. Yang, X. Duan, G. Hu, Q. Liu, S. Ren, J. Li, M. Kong, *Adv. Powder Technol.* **2020**, *31*, 4072; b) Z. Tan, J. Zhang, Y. C. Chen, J. P. Chou, Y. K. Peng, *J. Phys. Chem. Lett.* **2020**, *11*, 5390.
[118] Z. Li, W. Yang, L. Xie, Y. Li, Y. Liu, Y. Sun, Y. Bu, X. Mi, S. Zhan, W. Hu, *Appl. Surf. Sci.* **2021**, *549*, 149262.
[119] X. Shi, J. Yang, X. Wen, F. Tian, C. Li, *J. Rare Earths* **2020**, *39*, 1108.
[120] R. Maccarone, A. Tisi, M. Passacantando, M. Ciancaglini, *J. Ocul. Pharmacol. Ther.* **2020**, *36*, 376.
[121] H. Li, P. Xia, S. Pan, Z. Qi, C. Fu, Z. Yu, W. Kong, Y. Chang, K. Wang, D. Wu, *Int. J. Nanomed.* **2020**, *15*, 7199.
[122] M. Nadeem, R. Khan, K. Afridi, A. Nadhman, S. Ullah, S. Faisal, Z. U. Mabood, C. Hano, B. H. Abbasi, *Int. J. Nanomed.* **2020**, *15*, 5951.
[123] a) F. Charbgoo, M. B. Ahmad, M. Darroudi, *Int. J. Nanomed.* **2017**, *12*, 1401; b) S. Rajeshkumar, P. Naik, *Biotechnol. Rep.* **2018**, *17*, 1.
[124] a) Z. Liang, D. Jiang, G. Fang, W. Leng, P. Tu, Y. Tong, L. Liu, J. Ni, X. Li, *ChemistrySelect* **2019**, *4*, 4364; b) Q. Wei, Q. Ma, P. Zuo, H. Fan, S. Qu, W. Shen, *ChemCatChem* **2018**, *10*, 1019; c) K. Wu, X. Y. Wang, L. L. Guo, Y. J. Xu, L. Zhou, Z. Y. Lyu, K. Y. Liu, R. Si, Y. W. Zhang, L. D. Sun, *Nano Res.* **2020**, *13*, 2044.
[125] a) Z. Song, Y. Wei, X. Zhang, Y. Mao, J. Luo, X. Zhu, W. Liu, J. Jin, *Surf. Interfaces* **2021**, *24*, 101042; b) S. Mo, J. Li, R. Liao, P. Peng, J. Li, J. Wu, M. Fu, L. Liao, T. Shen, Q. Xie, *Chem. Eng. J.* **2021**, 129399.
[126] a) J. Liu, M. Hao, C. Chen, K. Du, Q. Zhou, S. Zou, L. Xiao, J. Fan, *Appl. Surf. Sci.* **2020**, *528*, 147025; b) L. Tan, T. Li, J. Zhou, H. Chen, F. Jiang, *Colloids Surf., A* **2018**, *558*, 211.
[127] K. M. Kumar, M. Mahendhiran, M. C. Diaz, N. Hernandez-Como, A. Hernandez-Eligio, G. Torres-Torres, S. Godavarthi, L. M. Gomez, *Mater. Lett.* **2018**, *214*, 15.
[128] a) V. Gurylev, T. P. Perng, *J. Eur. Ceram. Soc.* **2021**, *41*, 4977; b) J. Wang, R. Chen, L. Xiang, S. Komarneni, *Ceram. Int.* **2018**, *44*, 7357.
[129] a) S. A. Rawool, K. K. Yadav, V. Polshettiwar, *Chem. Sci.* **2021**, *12*, 4267; b) Z. Xiong, Z. Lei, Y. Li, L. Dong, Y. Zhao, J. Zhang, *J. Photochem. Photobio. C* **2018**, *36*, 24.
[130] a) Y. Lou, J. He, G. Liu, S. Qi, L. Cheng, J. Chen, Y. Zhao, J.-J. Zhu, *Chem. Commun.* **2018**, *54*, 6188; b) T. Paik, M. Cargnello, T. R. Gordon, S. Zhang, H. Yun, J. D. Lee, H. Y. Woo, S. J. Oh, C. R. Kagan, P. Fornasiero, *ACS Energy Lett.* **2018**, *3*, 1904.
[131] a) G. Li, Y. Mu, Z. Huang, N. Wang, Y. Chen, J. Liu, G. Liu, O. L. Li, M. Shao, Z. Shi, *Sci. China Mater.* **2021**, *64*, 73; b) H. Sun, C. Tian, G. Fan, J. Qi, Z. Liu, Z. Yan, F. Cheng, J. Chen, C. P. Li, M. Du, *Adv. Funct. Mater.* **2020**, *30*, 1910596; c) Y. Wang, Z. Chen, P. Han, Y. Du, Z. Gu, X. Xu, G. Zheng, *ACS Catal.* **2018**, *8*, 7113; d) L. Wu, S. Fang, L. Ge, C. Han, P. Qiu, Y. Xin, *J. Hazard. Mater.* **2015**, *300*, 93; e) X. Yu, J. Wu, A. Zhang, L. Xue, Q. Wang, X. Tian, S. Shan, C.-J. Zhong, S. Zeng, *CrystEngComm* **2019**, *21*, 3619; f) K. Schwarz, *Proc. Natl. Acad. Sci. U. S. A.* **2006**, *103*, 3497.



Chunming Yang received his B.S. degree in 2008 from the Qufu Normal University and his Ph.D. degree in 2019 from Jilin University. He currently works at Hunan University as a postdoctoral researcher under the supervision of Prof. Shuangyin Wang. His main research focuses on the electrocatalysis and electrocatalytic organic synthesis.



Yuxuan Lu received his B.S. degree in 2018 from the Department of Chemistry and Environment, Yunnan Minzu University, China. He is currently pursuing his doctoral degree under the supervision of Prof. Shuangyin Wang at Hunan University. His current interests include the design and synthesis of defect nanomaterials for green organic electrochemical synthesis.

© 2021 Wiley-VCH GmbH



Li Tao received his master's degree in 2016 and his Ph.D. degree in 2019 from Hunan University under the supervision of Prof. Shuangyin Wang. He is currently an assistant professor of the Key Laboratory for Graphene Materials and Devices and College of Chemistry and Chemical Engineering, Hunan University. His research interests are in plasma technology, defect chemistry, and fuel cell.



Yuqin Zou received her B.S. and M.S. degrees in 2012 from Shanghai University and her Ph.D. degree in 2016 from the University of Manchester, UK. She is currently a professor at the College of Chemistry and Chemical Engineering, Hunan University. Her research interests are in green electrochemical synthesis.



Shuangyin Wang received his bachelor's degree in 2006 from Zhejiang University and his Ph.D. degree in 2010 from Nanyang Technological University, Singapore. He is currently a professor at the Key Laboratory for Graphene Materials and Devices and College of Chemistry and Chemical Engineering, Hunan University. His research interests are defect chemistry of electrocatalysts, HT-PEMFC, and electrosynthesis.

© 2021 Wiley-VCH GmbH